IDŐJÁRÁS

QUARTERLY JOURNAL
OF THE HUNGARIAN METEOROLOGICAL SERVICE

CONTENTS

VOL. 98 * NO. 1 * JANUARY–MARCH 1994

IDŐJÁRÁS

Quarterly Journal of the Hungarian Meteorological Service

Editorial Office: P.O. Box 39, H–1675 Budapest

Subscription from customers in Hungary should be sent to the Financial Department of the Hungarian Meteorological Service Kitaibel Pál u. 1, 1024 Budapest. The subscription rate is HUF 2000.

Abroad the journal can be purchased from the distributor: KULTURA, P.O. Box 149, H–1389 Budapest. The annual subscription rate is USD 56.

IDŐJÁRÁS

Quarterly Journal of the Hungarian Meteorological Service
Vol. 98, No. 1, January–March 1994

Comparison of initialization methods in a barotropic model

I. Csigó[1] and **G. Radnóti**[2]

[1] *Department of Meteorology, Eötvös Loránd University, Ludovika tér 2, H-1083 Budapest, Hungary*
[2] *Hungarian Meteorological Service, Kitaibel Pál u. 1, H-1024 Budapest, Hungary*

(Manuscript received 10 December 1993; in final form 28 February 1994)

Abstract—This paper discusses the application and comparison of digital filter and nonlinear normal mode initialization within a one- and a two-dimensional barotropic model. The basic ideas of the compared initialization techniques and the short description of the applied models are presented together with some details of implementation.

Experiments made on the two models are discussed. The results prove that the recently developed digital filter initialization technique is an efficient method and can serve as a good alternative of the widely applied nonlinear normal mode initialization.

Key-words: initialization, digital filter, nonlinear normal modes, barotropic model.

1. Introduction

The aim of initialization of a numerical model is to remove spurious high frequency oscillations which could occur during the solution of primitive equation models. Since the first attempts on numerical weather prediction (NWP) numerous methods have been developed for eliminating these inertial-gravity waves (*Bengtsson*, 1975; *Daley*, 1981; *Daley*, 1991). Recently the most widely applied initialization method is the nonlinear normal mode initialization (NNMI), which was firstly introduced by *Machenhauer* (1977), and *Baer* and *Tribbia* (1977). Its relatively cheap computational costs and clear theoretical foundation are good reasons why this method has become almost uniquely used in most operational centers. Nevertheless, among other reasons, the increasing horizontal and vertical resolution, the more and more sophisticated parameterization of physical processes and the variety of vertical discretizations in recent NWP models raise some difficulties with NNMI, which

are mostly related to the stability and convergence of its iterative algorithm, the number and interpretation of initialized vertical modes and the inclusion of diabatic processes within the initialization procedure. A recently developed initialization based on digital filters (*Lynch* and *Huang*, 1992) being free of all these problems is therefore of particular interest. First experiments by the use of digital filter initialization (DFI) carried out in some NWP centres (such as the HIRLAM project of Northern European countries, the ARPEGE/ALADIN project of France and Central-Eastern-European countries, those at the Canadian Meteorological Service and at NOAA/FSL, USA) prove that, besides its extreme simplicity, the method is really efficient in removing gravity wave noises. Present paper intends to provide a short introduction of the method of DFI and to illustrate its effectiveness on a simple barotropic model. As a reference method to this experiment NNMI has been chosen.

2. The method of DFI

The basic idea of DFI is that high frequencies occuring in a time series can be filtered out if coefficients in the Fourier transform corresponding to these frequencies are set to zero and then the modified time series is recomputed by an inverse Fourier transform. This procedure formally means that the $F(\omega)$ Fourier transform of the function $f(t)$ is multiplied by the step function $H(\omega)$, where

$$H(\omega) = \begin{cases} 1, \; if \; |\omega| \leq |\omega_c|; \\ 0, \; if \; |\omega| > |\omega_c|. \end{cases} \tag{1}$$

It follows from the convolution theorem for Fourier series (*Folland*, 1992) that for the filtered function $f^*(t)$

$$f^*(t) = \int_{-\infty}^{\infty} h(\tau) f(t-\tau) \, d\tau \tag{2}$$

holds, where h is the inverse Fourier transform of $H(\omega)$, i.e.

$$h(t) = \frac{\sin(\omega t)}{\pi t}. \tag{3}$$

By the use of the discrete analogue of (2) and a truncation of the corresponding infinite sum at a level of N

$$f_n^* = \sum_{k=-N}^{N} h_k \, f_{n-k} \tag{4}$$

is obtained with

$$h_k = \frac{\sin(n\omega_c \Delta t)}{n\pi}. \tag{5}$$

To reduce the effect of Gibbs oscillation, which occurs due to the truncation of Fourier series, the weight function h can be multiplied by a window function, e.g. the well known Lanczos window function of the form of

$$w_n = \frac{\sin \frac{n\pi}{N+1}}{\frac{n\pi}{N+1}}. \tag{6}$$

Reduction of Gibbs oscillation can also be achieved by the use of an "optimum filter", which minimizes the distance between the step function (ideal filter response) and its reconstruction from finite elements in the Fourier series according to L_∞ norm. On the other hand, pure truncation minimizes the distance of the two responses in L_2 norm (*Huang* and *Lynch*, 1993).

3. The barotropic model

(a) 2-Dimensional case

For testing the algorithms of different initialization procedures and their filter efficiencies a tempting way is to implement the methods for a relatively simple model such as a 2-D barotropic model solving the shallow water equations, i.e. those governing the motion of an incompressible, homogeneous, non-viscous, quasi-static, rotating fluid with a flat bottom and a free top surface. These equations provide a closed system with 3 unknown variables, the horizontal wind components u, v and the geopotential height Φ

$$\partial_t u = -\partial_x K + (f+\xi)v - \partial_x \Phi + \sigma_u, \tag{7}$$

$$\partial_t v = -\partial_y K - (f+\xi)u - \partial_y \Phi + \sigma_v, \tag{8}$$

$$\partial_t \Phi = -u\partial_x \Phi - v\partial_y \Phi - \Phi D + \sigma_\Phi, \tag{9}$$

where ∂ represents partial derivatives according to its subscript, $K=0.5(u^2+v^2)$ is the kinetic energy, $D=\partial_x u + \partial_y v$ is the divergence and $\xi=\partial_x v - \partial_y u$ is the vorticity and σ represents any forcing term (in the basic case the only forcing taken into account is diffusion). Eqs. (7)–(9) do not contain diabatic terms, but in order to simulate diabatic processes, in some extent, σ was included which originates irreversibly in the model.

A simple spectral model integrating Eqs. (7)–(9) using double Fourier spectral representation for computing spatial derivatives and a semi-implicit leapfrog scheme for time discretization has been developed within the frame of the ARPEGE/ALADIN project in Toulouse, France and later implemented on a Hewlett Packard-710 workstation at the Weather Forecast Division of the Hungarian Meteorological Service. Initialization experiments have been carried out with different versions of NMI and DFI, both implemented for this model. Model experiments with simulating orographic and diabatic forcing have been also realized by modifying the basic equations, i.e. adding forcing terms to Eqs. (7)–(9).

(*b*) *1-Dimensional case*

To see the impacts of filter for an even simpler model, the 1-D version of the barotropic equations has also been coded. These equations are derived from system (7)-(9) by omitting derivatives with respect to y. This model, just like the 2-D one, computes derivatives in Fourier spectral space while the time discretization is carried out by an explicit leapfrog scheme. For initialization experiments different DFI versions have been implemented for this very simple model as well.

4. Implementation of digital filter and normal mode initialization techniques within the barotropic model

As it was mentioned above, DFI has been implemented both for the 1-D and for the 2-D version of the barotropic model while NMI only for the 2-D one. In this section details of implementation in the 2-D system will be discussed.

4.1 Implementation of DFI

An initialization using a non-recursive digital filter can be easily developed by using Eq. (2) for the initial time (n=0). Then the different filter "strategies" mean different choices of the h_k coefficients. Once this strategy is decided the set of h_k coefficients can be computed and stored in file. Then the application of Eq. (2) requires past and future model states around the initial time. This can be achieved by backward and forward integration of the model starting from the original initial state and applying Eq. (2) for each prognostic variable at each gridpoint independently.

In the case of adiabatic DFI (ADFI) both backward and forward integrations are carried out without diabatic terms. Thus the steps of ADFI procedure can be summarized as

– adiabatic backward integration from $t=0$ to $t=-T/2$;

- adiabatic forward integration from $t=0$ to $t=T/2$, starting from the original initial fields.

During the backward and forward integration the filtered state is being accumulated by adding the current state with the current weight to the sum, as prescribed by Eq. (2).

When the filter is diabatic (DDFI) the procedure described above needs some modification because diabatic processes can't be taken into account during backward integration. In this case the procedure starts with an adiabatic backward model integration just to establish the starting state from where the forward diabatic integration will start and the accumulation of the filtering sum will be realized along the forward diabatic model trajectory. This can be summarized in the following points

- adiabatic backward integration from $t=0$ to $t=-T/2$ without accumulation of filter sum;
- diabatic forward integration from $t=-T/2$ to $t=T/2$ with accumulation of filter sum.

It should be remarked that the diabatic forward trajectory, which follows the adiabatic backward one and starts from the endpoint of the backward one, does not exactly pass through the original initial state. Though this brings some inaccuracy into the procedure, the benefit of inclusion of diabatic processes is much more important, especially for a model with sophisticated physics in it. All this is not expected to be proven by such a simple barotropic model where the only irreversible process is horizontal diffusion.

4.2 Implementation of NMI

To have reference for evaluating the performance of DFI, NMI has also been implemented for the 2-D barotropic model. The method, which has been applied, is based on Machenhauer's explicit algorithm (*Machenhauer*, 1977). For the present barotropic spectral model this can be summarized as follows. Let

$$\underline{X} = \begin{pmatrix} u \\ v \\ \Phi \end{pmatrix} \tag{10}$$

denote the state vector of the model. Then the evolution equation of the model can be written as

$$\frac{d\underline{X}}{dt} = F(\underline{X}) = L(\underline{X}) + N(\underline{X}), \tag{11}$$

where L represents the linear and N the nonlinear part of the model. For the

barotropic model this decomposition of the vector field $F(\underline{X})$ can be of the form

$$\underline{\underline{L}} = \begin{pmatrix} 0 & f & -\partial_x \\ -f & 0 & \partial_y \\ -\Phi_0\partial_x & -\Phi_0\partial_y & 0 \end{pmatrix}, \tag{12}$$

where f is the Coriolis parameter and Φ_0 is the reference geopotential height. In the case of bi-Fourier spectral representation the operator $\underline{\underline{L}}$ can be considered separately for each wavenumber-pair (m,n) and can be written as

$$\underline{\underline{L}}^{(m,n)} = \begin{pmatrix} 0 & f & -ikm \\ -f & 0 & iln \\ -ikm\Phi_0 & -iln\Phi_0 & 0 \end{pmatrix}, \tag{13}$$

where i is the imaginary unit, $k=2\pi/L_x$, $l=2\pi/L_y$ and L_x and L_y are the sizes of the model domain in x and y directions, respectively. The normal modes of the linearized system are the eigenvectors of $\underline{\underline{L}}$, which can be decomposed into rotational and gravity modes, here defined as eigenvectors corresponding to zero and non-zero eigenvalues, respectively. For the operators in (13) the eigenvalues are

$$\mu_1^{(m,n)} = 0, \quad \mu_{2,3}^{(m,n)} = \pm i\sqrt{l^2n^2\Phi_0 + k^2m^2\Phi_0 + f^2} \tag{14}$$

and the corresponding eigenvectors are the columns of the eigenvector matrix

$$\underline{\underline{W}}^{(m,n)} = \begin{pmatrix} -inl & km\lambda - inlf & -km\lambda - ilnf \\ ikm & nl\lambda + ikmf & -nl\lambda + ikmf \\ f & -l^2n^2\Phi_0 - k^2m^2\Phi_0 & -l^2n^2\Phi_0 - k^2m^2\Phi_0 \end{pmatrix}, \tag{15}$$

where

$$\lambda = \sqrt{l^2n^2\Phi_0 + k^2m^2\Phi_0 + f^2}. \tag{16}$$

To get the normed form of $\underline{\underline{W}}$ the first column must be multiplied by

$$1/[l^2n^2 + k^2m^2 + f^2)^{0.5}]$$

while the second and third columns both by

$$1/[\{k^2m^2\lambda^2 + l^2n^2f^2 + l^2n^2\lambda^2 + k^2m^2f^2 + (l^2n^2\Phi_0 + k^2m^2\Phi_0)^2\}^{0.5}].$$

The normal modes span the whole phase space of the truncated system (here

truncation means that finite number of m and n is considered) and they provide a basis in the phase space determining two linear manifolds G and R spanned by the gravitational and rotational normal modes respectively.

When performing linear normal mode initialization (LNMI), the initial states are chosen from the manifold R, i.e. an arbitrary initial state vector is projected onto R. Due to the presence of the nonlinear part N of the model, however, this choice of initial state does not guarantee that during the temporal evolution of the system the phase space trajectory remains within R. Therefore, in the case of NNMI, instead of this, an initial state for which

$$\left[\frac{d\underline{X}}{dt}\right]_G = 0 \tag{17}$$

is prescribed, where the subscript G represents projection of any vector in the phase space onto the manifold G. The iteration procedure given by

$$\underline{X}_G^{(p+1)} = \underline{X}_G^{(p)} - L_G^{-1}\left(\frac{d\underline{X}^{(p)}}{dt}\right)_G ; \quad \underline{X}_R^{(p+1)} = \underline{X}_R^{(p)} , \tag{18}$$

where the subscript R represents the projection of any vector in the phase space onto the manifold R, provided it converges, leads to a state satisfying the above requirement and at the same time the iteration does not touch rotational modes. In Eq. (18) L_G represents the linear transformation of the manifold G for which $L_G(\underline{y})=L(\underline{X})_G$, $\underline{y} \in G$ where $\underline{X}$ is the vector in the phase space for which $\underline{X}_G=\underline{y}$ and $\underline{X}_R=0$. In each iteration step the tendencies on the right hand side of the first Eq. of (18) can be derived by a single timestep integration of the model with Eulerian explicit tendencies. In this case with $\Delta t=1$, the differences between the fields gained after and before a single timestep Eulerian explicit integration of the model directly provide the desired tendencies. The correction term for one iteration step can be written for each wavenumber-pair as

$$(\underline{X}^{(p+1)} - \underline{X}^{(p)})^{(m,n)} = -\underline{\underline{W}}^{(m,n)} \begin{pmatrix} 0 & 0 & 0 \\ 0 & 1/\mu_2{}^{(m,n)} & 0 \\ 0 & 0 & 1/\mu_3{}^{(m,n)} \end{pmatrix} \underline{\underline{W}}^{(m,n)^{-1}} \frac{d\underline{X}^{(p)(m,n)}}{dt} . \tag{19}$$

This transformation of the tendency vector is a sequence of three linear operations, which are

- a basis transformation from the basis of spectral prognostic variables to that of normal modes;
- transformation representing the correction term of an iteration step written in the transformed (normal mode) space;
- inverse basis transformation.

It should be noted that this transformation can be carried out in the same manner for each wavenumber-pair, except for (0,0), for which the eigen-problem has only one nontrivial solution and this corresponds to the rotational mode. It means that the iteration procedure does not touch this wavenumber-pair, involving that field-averages remain unchanged during the initialization.

In the LNMI case the initialization formula is non-iterative and can be written as

$$\underline{X}^{(m,n)}_{initialized} = \underline{X}^{(0)(m,n)} - \underline{\underline{W}}^{(m,n)} \begin{pmatrix} 0 & 0 & 0 \\ 0 & 1 & 0 \\ 0 & 0 & 1 \end{pmatrix} \underline{\underline{W}}^{(m,n)-1} \underline{X}^{(0)(m,n)} . \qquad (20)$$

As the tranformation matrices in (19) and (20) depend only on the geometry of the model and the reference geopotential height, they can be computed and stored preliminarily to model run. The major steps of NNMI can be summarized as

- one timestep integration of the model;
- computation of tendencies of prognostic variables;
- sequence of direct FFT-s (Fast Fourier Transformation) to transform tendencies to spectral space;
- computation of correction terms;
- inverse FFT-s;
- convergence test;
- updating prognostic fields.

These steps for LNMI are very similar, just the multiplier matrix is of different form and there is no iteration.

5. Results

In this section the results of digital filtering technique and its comparison with those of the nonlinear normal mode technique will be described for the above mentioned two models.

5.1 1-Dimensional case

This model works over the whole latitudinal circle 45°N with 72 grid points. Thus the resolution is 393.6 km (5°). The time step for the integration is 8 minutes, which satisfies the Courant-Friedrichs-Lewy condition. The filter span is chosen to be 8.6 hours and the filter coefficients are calculated according to optimum filter.

To demonstrate the efficiency of DFI technique the model was integrated from different initial conditions. The time evolution of geopotential height for the first 24 hours (180 time steps) of two different initial conditions at a certain grid point is shown in *Figs. 1* and *2*. The mean initial geopotential height is

30,000 J/kg. The wind components were derived by adding an analytical ageostrophic term to the geostrophic wind components. The uninitialized trajectory shows that the high frequency oscillations are not damped during the time integration so the 1-D model itself is not able to adjust mass and momentum fields. In Fig. 2 a strong initial "shock" can be observed at the examined gridpoint and this effect together with the high frequency noises are successfully removed by DFI. The curves corresponding to DFI also prove that lower frequency oscillations are not removed by DFI and that the separation of waves is well controlled by DFI parameters: stop and pass edges of optimum filter were chosen to be 3 and 12 hours respectively and this is in agreement with the results in Figs. 1 and 2, which show that the highest frequencies occuring after DFI are of the order of 50 timesteps (6.5 hours).

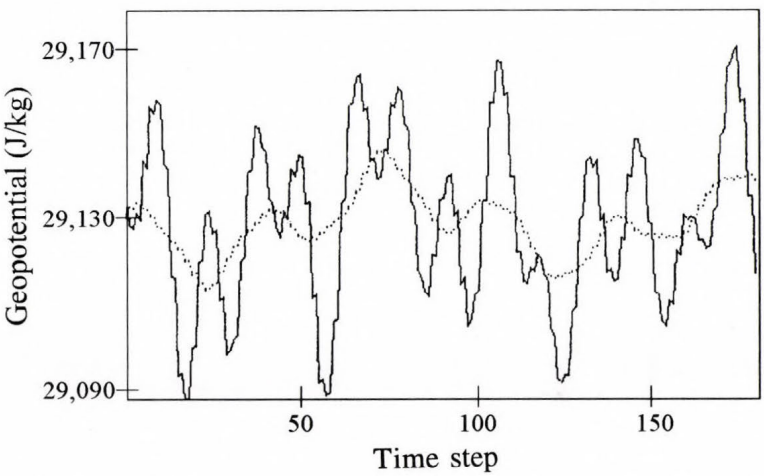

Fig. 1. Time evolution of geopotential height at a certain grid point gained by the 1-D model without initialization (solid line) and with DFI (dotted line).

5.2 2-Dimensional case

This model is launched over a 64×36 point grid with cca 50 km resolution in both directions and the timestep is 5 minutes. The Coriolis parameter is assumed constant. The DFI time span is 8.3 hours and the filter coefficients are determined by Lanczos windowing with a 6 hour cutoff period. Periodic lateral boundary values are applied in both directions by this making possible the bi-Fourier spectral representation. The mean geopotential value is 30,000 J/kg.

The first experiment shown in this paper starts from simple geostrophic initial conditions (*Fig. 3*). The initial field corresponding to this experiment varies in x and y direction as well. The geostrophic initial condition is produced by adjusting the initial wind field to the geopotential field. The two curves in Fig. 3 represent the time evolution of geopotential height for the first 288 time steps (24 hours) starting from initialized and uninitialized initial fields. The

smooth curve represents in fact two cases, one gained by DFI and another gained by NNMI, but they evolve completely identically. It is important to distinguish the two sorts of NMI procedures, the linear and nonlinear one, because in this case they yield significantly different solutions (LNMI does never make any modification on geostrophic initial conditions). As it can be

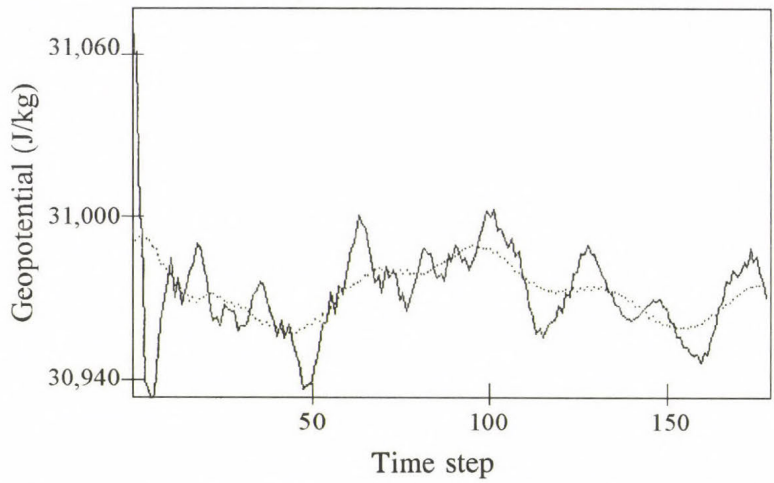

Fig. 2. Time evolution of geopotential height at a certain grid point gained by the 1-D model in uninitialized case (solid line) and initialized with DFI (dotted line).

seen in Fig. 3, in contrast with the 1-D results, gravity wave oscillations are damped by the model as the time evolves. Some further experiments were made with one-dimensional initial fields, i.e. for which initial fields vary only in x direction.

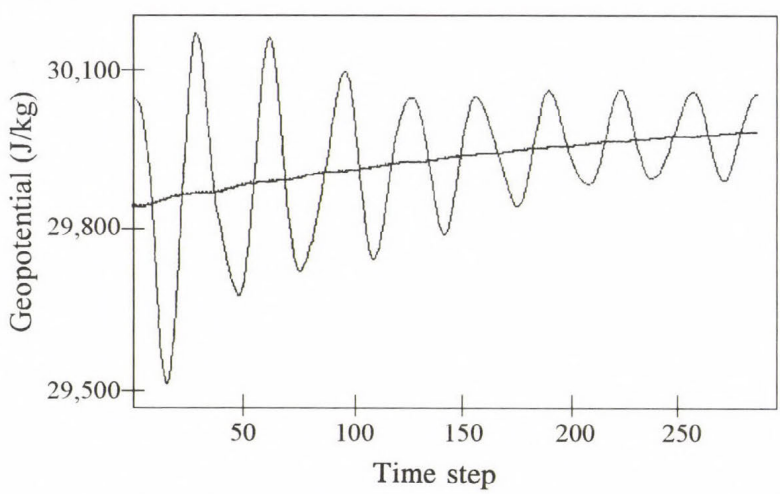

Fig. 3. Time evolution of geopotential height at a central grid point of the 2-D model domain in unfiltered (solid line) and initialized NMI and DFI (smooth line) cases.

After establishing the fields satisfying geostrophic relationship the geopotential field was modified in the central region of the domain (*Fig. 4a*). As it is seen in *Figs. 4b, c*, the two kinds of initialization simply remove this perturbation from the geopotential field setting back the original one-dimensional field. *Fig. 4d* shows the corresponding evolution of geopotential height at a gridpoint within the area of perturbation and this figure indicates that both initializations exhibit good filter efficiency. It should be remarked that this initial state would involve stationary solution if there were no horizontal diffusion in the model.

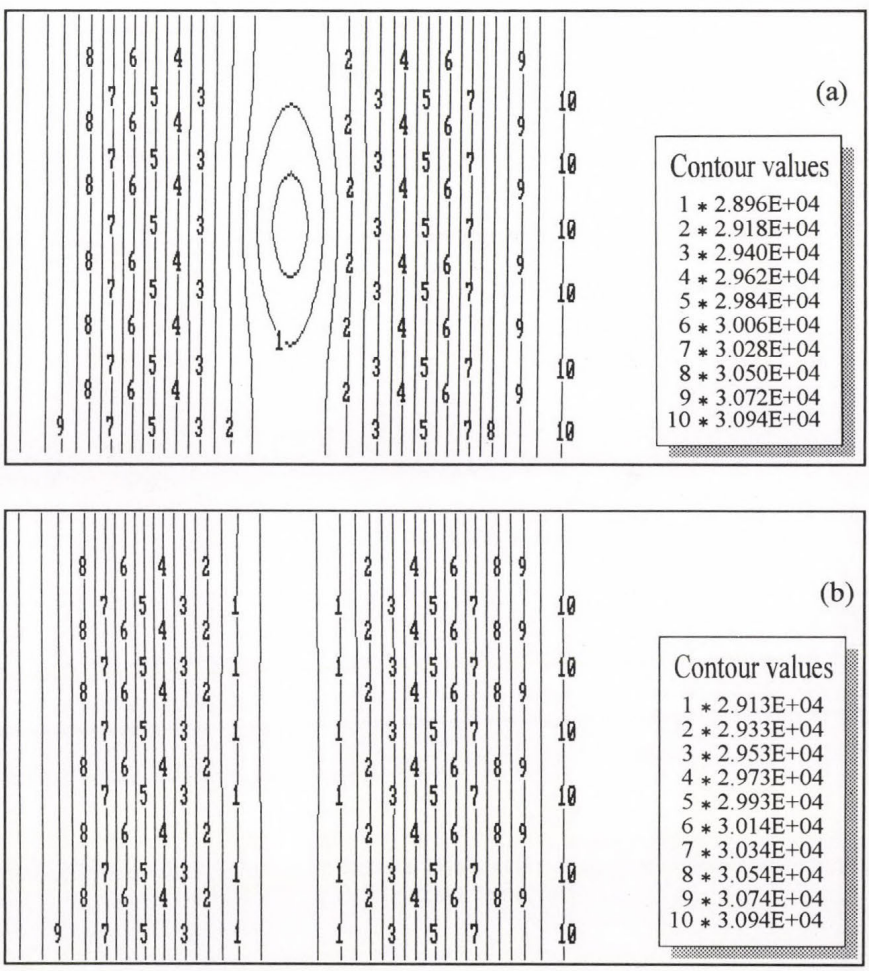

Fig. 4a, b. Initial geopotential field of the 2-D model gained by (*a*) no initialization, (*b*) DFI.

The experiment presented in *Fig. 5a, b* also applies a one-dimensional basic state, but now the introduced perturbation consists of a single gridpoint

disturbance and a superposed noise. In the uninitialized case this involves a strong initial "shock". DFI and NMI removes this shock as well as the high frequency oscillations from the evolution.

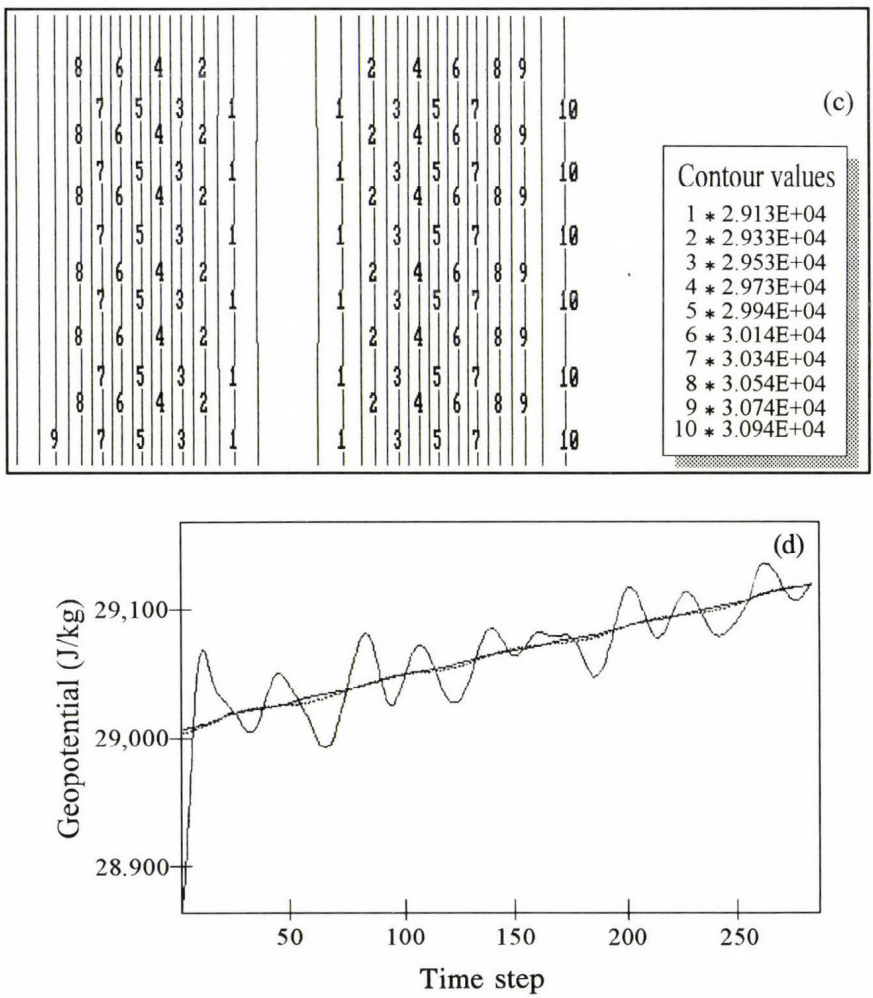

Fig. 4c, d. Initial geopotential field of the 2-D model gained by (*c*) NNMI, (*d*) the corresponding time evolutions at a single grid point of the domain: no initialization (solid line), DFI (dotted line) and NNMI (smooth solid line).

6. Summary and concluding remarks

The aim of the experiments presented in this paper was to get an idea about the applicability of the recently developed digital filter initialization technique. The vehicle for this experiments were simple one- and two-dimensional

barotropic models. Unbalanced initial fields were created and DFI and NMI methods were used to remove gravity wave noises.

All the experiments described in this paper show very similar performance of NNMI and DFI. This proves that the ideas behind digital filter work well in practice and the technique is adequate for initialization purposes in numerical weather prediction.

However, in order to see more specific properties of the method, with especial regard to diabatic aspects, one probably has to carry out experiments on a more realistic prognostic model with sophisticated physical parameterization.

Acknowledgments – Present study is based on the model developed within the frame of the ALADIN project of METEO-FRANCE and some Central-Eastern-European meteorological services. We thank all ALADIN staff and project leaders for the support.

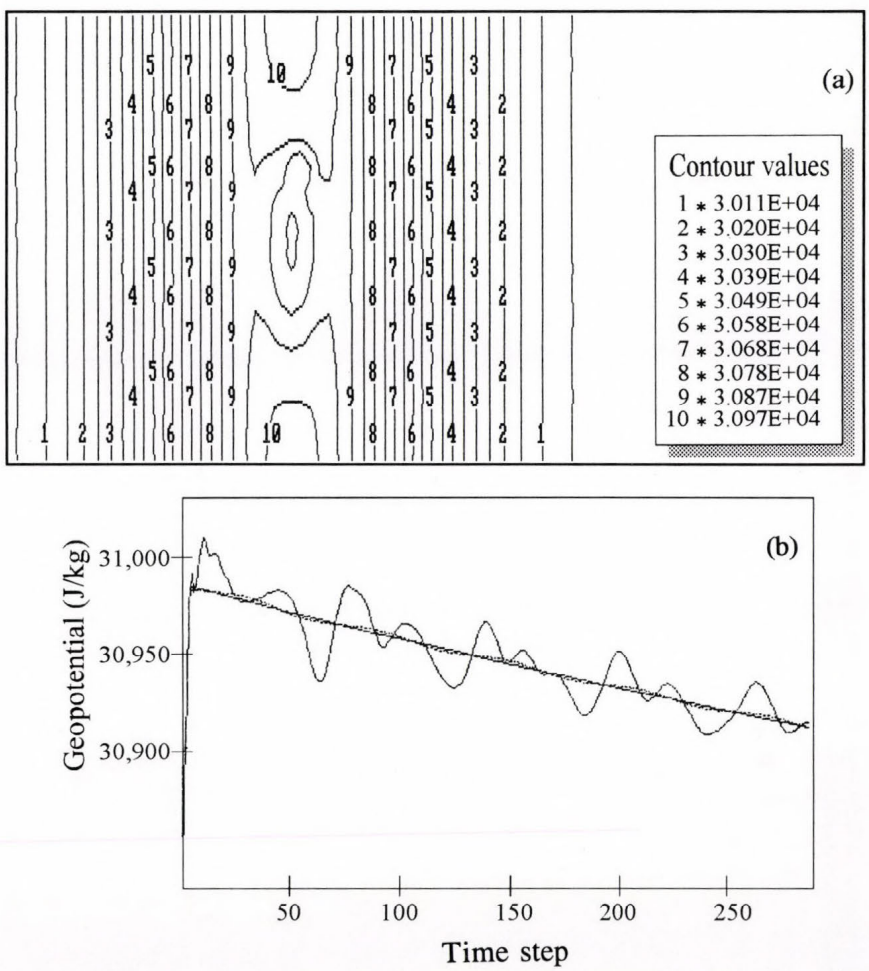

Fig. 5. (*a*) Initial geopotential field of the 2-D model, (*b*) time evolution at a single gridpoint without initialization (solid line), with NNMI (smooth solid line) and DFI (dotted line).

References

Baer, F., 1977: Adjustment of initial conditions required to suppress gravity oscillations in non-linear flows. *Beitr. Phys. Atmos. 50*, 358-366.

Baer, F. and *Tribbia, J.*, 1977: On complete filtering of gravity modes through nonlinear initialization. *Mon. Wea. Rev. 105*, 1536-1539.

Bengtsson, L., 1975: 4-dimensional assimilation of meteorological observations. *GARP Publ. Ser.*, No. 15. *WMO/ICSU Joint Organizing Committee.*

Daley, R., 1981: Normal mode initialization. *Rev. Geophys. Space Phys. 19*, 450-468.

Daley, R., 1991: *Atmospheric data analysis*. Cambridge University Press, Cambridge.

Folland, G.B., 1992: *Fourier analysis and its applications*. Wadsworth and Brooks/-Cole, Pacific Grove.

Huang, X.Y. and *Lynch, P.*, 1993: Diabatic digital-filtering initialization: application to the HIRLAM model. *Mon. Wea. Rev. 121*, 589-603.

Lynch, P. and *Huang, X.Y.*, 1992: Initialization of the HIRLAM model using a digital filter. *Mon. Wea. Rev. 120*, 1019-1034.

Machenhauer, B., 1977: On the dynamics of gravity oscillations in a shallow water model with application to normal mode initialization. *Beitr. Phys. Atmos. 50*, 253-271.

IDŐJÁRÁS

Quarterly Journal of the Hungarian Meteorological Service
Vol. 98, No. 1, January–March 1994

Air cleaning by low frequency acoustic wave

A. Sadigzadeh

Radiation Protection Department, Atomic Energy Organization of Iran
P.O. Box 14155-4494, Tehran, Iran

(Manuscript received 10 February 1994)

Abstract—The aim of this work is to study the granular beds, with and without an acoustic wave used in air cleaning processes. In the absence of an acoustic field our experimental results are in a good agreement with the theory developed by *Otani et al.* (1989). In the presence of a high acoustic pressure level (APL $\geq$ 130 dB), our experiments show an increase in granular bed efficiency. The efficiency shows a large rise from a threshold value in acoustic pressure level.

Key-words: granular bed, filter efficiency, acoustic wave.

1. Introduction

Sonic treatment of aerosol particles in waste gases is an advanced industrial emission control technique. Under the high-temperature, high pressure, corrosive and explosive environment, the necessity for elimination of the aerosols makes the acoustic filter one of the primary gas cleaning devices. The depressurization of the enclosure at high pressure (nuclear industry), residual particle removal in the inflammable environment (petroleum and combustible gas industry), etc. are the examples of recent application of acoustic gas cleaning devices. An acoustic filter is composed of two parts (*Fig. 1*):

(1) an acoustic agglomeration chamber (AAC),

(2) a granular bed.

Application of acoustic waves increases the kinetic energy of aerosol particles in the gas medium. This becomes important above a certain threshold value in acoustic pressure level, it increases the probability of the collisions between the particles themselves, and the obstacles. The acoustic field increases the efficiency of an acoustic filter at two stages:

– An increase of aerosol particles diameter by increasing coagulation

factor, for example, with an acoustic field of f=1 kHz, APL=165 dB, the increase of the diameter of the initial monodisperse aerosol particles (D_p=3.34 μm) by a factor of 3 (*Malherbe,* 1987).

– An increase in the overall efficiency of the granular bed, by increasing the aerosol particles diameter and by adding an important aerosol capture mechanism due to the induced force in the medium which acts on the aerosol particles.

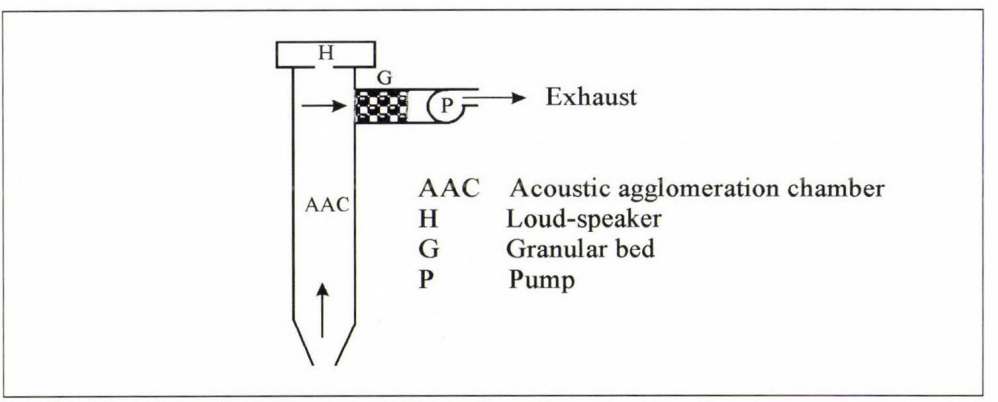

Fig. 1. The schematic diagram of an acoustic filter.

2. Efficiency of a granular bed

The theoretical expression for the capture efficiency of the aerosol particles (E) by a granular bed is a function of its depth (L) and porosity (ε), as well as the diameter (D_s) and the total single collector efficiency η_t of spherical collectors (*Tardos et al.*, 1974)

$$E = 1 - \exp\left[-\frac{3(1-\varepsilon)L}{2\,\varepsilon\,D_s}\eta_t\right]. \tag{1}$$

If we neglect the interactions between the different collection mechanisms, electrostatic and sieve effect; η is obtained by adding the contribution of individual collection mechanisms: sedimentation (η_s), inertial impact (η_{imp}), direct interception (η_i) and diffusion (η_d). Consequently

$$\eta_t = \eta_s + \eta_{imp} + \eta_i + \eta_d. \tag{2}$$

In the absence of an acoustic field, our experimental results agree with the theoretical results developed by *Otani et al.* (1989) and by *Sadigzadeh* (1989). In the relations 3 to 6, the principal expressions are summarized

$$\eta_I = \frac{St_{eff}^{\ 3}}{0.014 + St_{eff}^{\ 3}}, \tag{3}$$

where

$$St_{eff} = \left[1 + \frac{1.75\,Re\,(1-\alpha)}{150\alpha}\right] St,$$

$$\eta_{Int} = 16R^{\left(2 - \frac{Re}{Re^{1/3}+1}\right)^3}, \tag{4}$$

$$\eta_s = \frac{G}{1+G}, \tag{5}$$

$$\eta_D = 8\,Pe^{-2/3} \quad \text{for } Re \to 0, \qquad \eta_D = 2.1\,Pe^{-1/2} \quad \text{for } Re \to \infty. \tag{6}$$

(The denotations are explained at the end of the paper.)

3. The effect of the acoustic field on aerosol particles

Application of an acoustic wave with a level more than 130 dB generates the occurrence of a number of complex and violent motions by the particles, in addition to the motions such as Brownian or settling that a particle has in a gas medium. This is due to the fact that the particles take some part in the vibration of the gas, in the translation motion or "drift" and acoustic turbulence induced by the acoustic field in the gas. These phenomena act on the suspended particles and affects their movements.

The motion of the aerosols in a vibrating carrier gas can be described by the entrainment factor μ_p (*Mednikov,* 1965). For an isolated spherical particle of aerodynamic diameter D_p moving in a sonic field of frequency (f), the entrainment factor is

$$\mu_p = \frac{A_p}{A_g} = \frac{1}{(1+\omega^2\tau^2)^{1/2}}, \tag{7}$$

where A_p, A_g are the amplitude of a particle and gas vibration in the acoustic wave, while $\omega(\omega=2\pi f)$ and $\tau(\tau=\rho_p D_p^{\ 2}/18\eta_g)$ denote the angular frequency of the acoustic wave and the relaxation time of the aerosol, respectively. According to the angular frequency we can differentiate the following cases:

- $\omega\tau \ll 1$, in this case, the amplitude of acoustic oscillations of an aerosol and of the carrier gas molecules are equal ($A_p \approx A_g$).
- $\omega\tau \gg 1$, in this case, $A_p \approx 0$.

Above the pressure level of 158 dB (see *Cheng et al.*, 1983; *Boulaud et al.*, 1984), the acoustic turbulence becomes important enough to induce a force that

favours the probability of collision between the particles, and the particles and an obstacle such as an element of the constituent media. The overall efficiency of the granular media in the presence of an acoustic field (E_T) is given by the following relation

$$E_T = 1 - \exp\left[\frac{3(1-\varepsilon)}{2\varepsilon D_s}\eta_T L\right]; \quad \eta_T = \eta_t + \eta_{ac}, \tag{8}$$

where η_T is the total single collector efficiency in the presence of an acoustic wave, while η_{ac} is the acoustic efficiency of a spherical collector; this is dependent on the frequency and sound pressure level of the acoustic waves and the spherical collector and particles size.

4. Experimental apparatus and measurement

The schematic diagram of the experimental set up is shown in *Fig. 2*. The granular bed used consisted of spherical glass collectors. This was set up inside of a glass column of 1 m height and 6.7 cm internal diameter. In our experiments, we used monodisperse aerosols of dioctyle phtalate (DOP) and dioctyle sebacate (DES) produced by a two stage aerosol generator (TSI; model 3072, and 3076) and a MAGE (for particles larger than 1 μm), respectively. The acoustic waves are generated by a high power loud-speaker (maximum effective power 120 watts). The sinusoidal signal is fed by an electric signal generator, and amplified by an audio-amplifier before supplying the loud-speaker.

An original dilution system *Sadigzadeh* (1989), allows us to produce aerosol concentrations ranging from a few to 10^5 particles/cm^3. A pump assures the

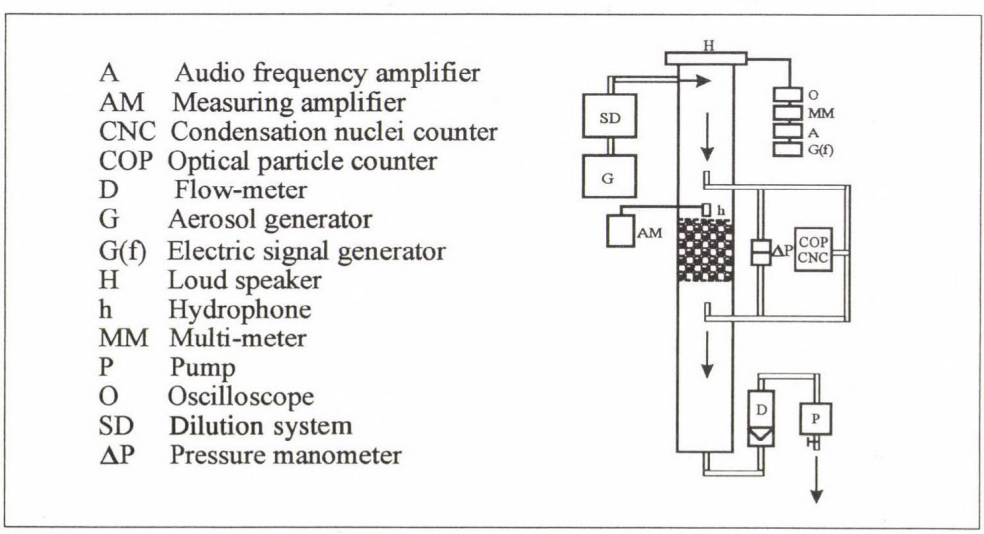

Fig. 2. Experimental device.

clean air circulation in the device. The shape and the power of yielded signal to the loud-speaker is monitored by an oscilloscope and a voltage, and an intensity multimeters. The acoustic pressure level (APL) is measured by a Bruel & Kjær system comprising a hydrophone, a pre-amplifier (BK 2626) and a reading amplifier (BK 2609). The upstream and downstream aerosol volume concentration and size distribution of particles were determined by a condensation nuclei counter (TSI), an optical particle counter (Kratel) and a quartz crystal micro-balance cascade impactor (California measurements INC).

The pressure drop was obtained with and without acoustic wave by a pressure manometer.

5. Experimental results

5.1 Electrical power

The effective electrical power necessary to supply the loud-speaker for obtaining an acoustic field by a given APL was determined. For example, in an experiment a granular bed with following characteristics: L=20 cm, D_s=5 mm and ε=0.38 was made. *Fig. 3* shows the increase of the APL measured in a loop of the acoustic pressure as a function of the effective electrical power supplied to the loud-speaker. The frequencies chosen were those of resonance frequencies of the set-up. For example, we observed that for a fixed frequency of 450 Hz, 24 W effective electrical power is enough for obtaining 160 dB of APL.

5.2 Pressure drop

The pressure drop ΔP of a granular bed rises with the flow rate. In the presence of an acoustic wave, the pressure drop increases. This is in direct proportion to APL and inversely proportional to acoustic frequency. As an example, *Fig. 4* shows the increase of the pressure drop of a granular bed (L=20 cm, D_s=2 mm, ε=0.39), as a function of the APL, for three different frequencies.

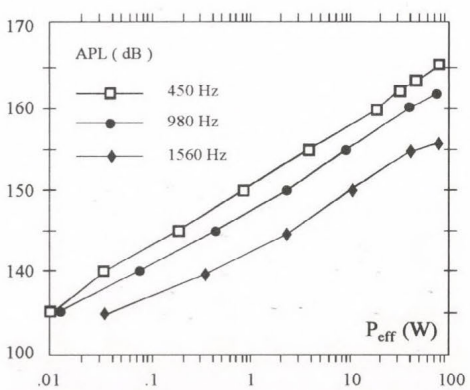

Fig. 3. Acoustic pressure level, versus the effective electric power (P_{eff}).

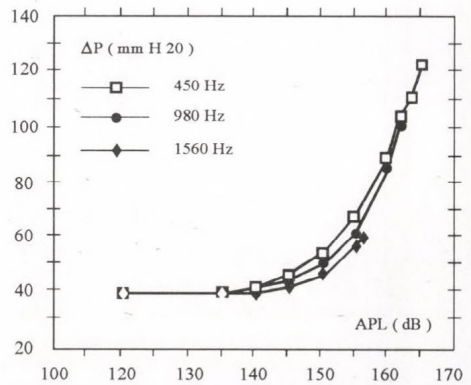

Fig. 4. The pressure drop of the granular bed versus the APL. U_f=18 cm s^{-1}.

5.3 *Efficiency of a granular bed*

We verify our theoretical forecast, by developing a number of experiments to measure the efficiency of the granular bed with and without an acoustic field. The efficiency of different granular beds (L=20 cm, D_s=1, 2 and 5 mm), is determined experimentally for different carrier gas velocities: 4.5, 9, 18 cm s^{-1}. The diameter of DES monodisperse aerosol particles used, are 2,3.3 and 4 μm. In these experiments, the generated acoustic wave frequencies are successively fixed at 450, 980 and 1590 Hz; the APL varies in the range 120 and 164 db.

In *Fig. 5* typical data are illustrated showing the increase in the efficiency of the granular bed (L=20 cm, D_s=2 mm, ε=0.39) as a function of the APL. For two air velocities, the diameter of the monodisperse aerosol used was 2 μm. The acoustic wave frequency was fixed at 450 Hz. The experimental data indicate that the action of acoustic wave on granular bed increases with air flow rate. Our explanation for this phenomena is as follows. The expansion of the turbulent volume because of the transport of the acoustic vortex is locally induced by the carrier gas movement.

The increase of the granular bed (L=20 cm, D_s=5 mm, ε=0.38) efficiency in the presence of an acoustic field of frequency 450 Hz, for three different particle diameters is illustrated in *Fig. 6*. The velocity of air is fixed at 4.5 cm s^{-1}. We observe an increase in the efficiency of granular bed by the APL. There is a great increase from a threshold APL, which is dependent on the aerosol particle size, for the particles of 2, 3.3, 4 μm diameter, this threshold is situated at 150, 145 and 145 dB, respectively.

In order to evaluate the effect of the acoustic wave on the capture efficiency of fine particles by a granular bed, a new series of experiments was carried out to measure the efficiency of a granular bed (L=15 cm, D_s=2 mm, ε=0.39) in

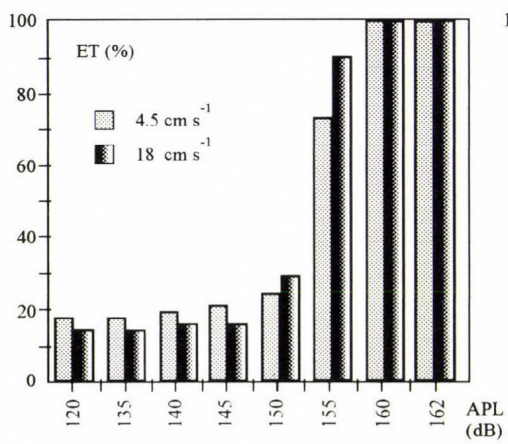

Fig. 5. The overall efficiency of the granular bed versus APL, for different air velocity.

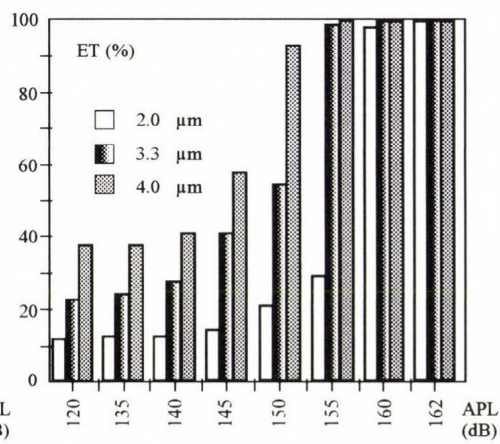

Fig. 6. The overall efficiency of the granular bed, versus APL, for different diameters of aerosol. U_f=4.5 cm s^{-1}.

the presence of an acoustic field for the submicrometric aerosol particles. The velocity of air flow rate was fixed at 7.9 cm s^{-1}, and the diameter of the DOP monodisperse aerosol particles used were 0.1, 0.5, 1 μm. The studied frequencies were 0.2, 0.5, 1, 1.5, 2, 2.5, 3 kHz, and the acoustic pressure level varied in the range of 120–160 dB.

By virtue of example in the histogram of *Fig. 7* the efficiency increase of the granular bed is plotted as a function of APL for the frequency fixed to 1 kHz. The experimental histogram allows us the following comments:

- The acoustic wave act on the efficiency of granular bed from 130 dB, in the diffusional range (D_p=0.1 μm), from 140 dB in the intermediary range (D_p=0.5, 1 μm).
- The acoustic impact on the efficiency is more important for large particles.

6. Conclusions

Our theoretical and experimental exploration for the various air velocities, spherical collector diameters and particle sizes, demonstrate the following results

- Without acoustic waves, our experimental results are in a good agreement with the theory of *Otani et al.* (1989).
- Under the effect of a high acoustic pressure level, the efficiency of a granular bed rises substantially. It is demonstrated that from a threshold in APL, the increase of granular bed efficiency is greater.
- The acoustic impact on granular bed efficiency is more important for large aerosol particles and for spherical collectors of small diameter.
- From 160 dB in acoustic pressure level, the efficiency of the studied granular bed exceeds 97% for the particles of diameter $\geq$0.5 μm.
- The pressure drop of granular bed rises in the presence of an acoustic field. Nevertheless, this was not too high to be used for the industrial filtering application.

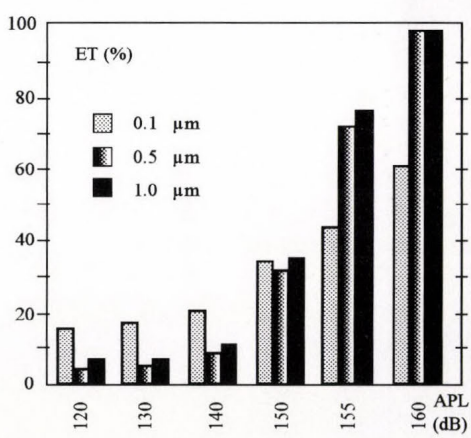

Fig. 7. The overall efficiency of a granular bed (L=15 cm, D_s=2 mm), versus APL. U_f=7.8 cm s^{-1}.

Acknowledgements—I wish to thank *Professor A. Renoux* for the helpful suggestions and discussions.

List of symbols

C Cunningham slip correction
D_s spherical captor diameter
G sedimentation parameter $=2g\rho_p D_p/9\eta_g U_f$
K_B Boltzmann's constant
Pe Peclet number $=D_s U_f/D_B$
Re Reynolds number $=D_s U_i/\nu$
St_{eff} effective Stokes number
U_i interstitielle air velocity $=U_f/\varepsilon$
α solid fraction of bed $=1-\varepsilon$
ε porosity of bed
ν_g kinematic viscosity of carrier gas
τ relaxation time of particle $=2\rho_p R_p^2/9\eta_g$
D_B particle diffusion coefficient $=CK_BT/3\pi\eta_g D_p$
f acoustic frequency
g acceleration of gravity
L depth of granular bed
R interception parameter $=D_p/D_s$
St Stokes effective number $=C\rho_p D_p^2 U_i/9\eta_g D_s$
T temperature
U_f superficial velocity
ΔP pressure drop
η_g fluid viscosity $=\nu_g\rho_g$
ρ_p particle density.

References

Boulaud, D., Frambourt, C., Madelaine, G. and *Malherbe, C.*, 1984: Experimental study of the acoustic agglomeration and precipitation of an aerosol. *J. Aerosol Sci. and Technol. 15*, 247-252.

Cheng, M.T., Lee, P.S., Berner, A. and *Shaw, D.T.*, 1983: Orthokinetic agglomeration in an intense acoustic field. *J. of Coll. and Interface Sci. 91*, 176-187.

Malherbe, C., 1987: Etude du comportement d'un aérosol soumis à un champ sonore. Thèse de doctorat d'état. Université Paris XII.

Mednikov, E.P., 1965: *Acoustic Coagulation and Precipitation of Aerosols*. Consultants Bureau, New York.

Otani, Y., Kanaoka, C. and *Emi, H.*, 1989: Experimental study of aerosol filtration by the granular bed over a wide range of Reynolds numbers. *J. Aerosol Sci. and Technol. 10*, 463-474.

Sadigzadeh, A., 1989: Filtrate acoustic. *6. Journées d'études sur les aérosols* (COFERA), 45-50.

Tardos, G., Gutfinger, C. and *Abuaf, N.*, 1974: Deposition of dust particles in a fluidized bed filter. *Israel J. Technol. 19*, 184-189.

IDŐJÁRÁS

Quarterly Journal of the Hungarian Meteorological Service
Vol. 98, No. 1, January–March 1994

The spectral reflection of different soils and soil ingredients

G. Szász and **V. Zilinyi**

Debrecen Agricultural University,
P.O. Box 36, H-4015 Debrecen, Hungary

(Manuscript received 5 October 1993; in final form 28 January 1994)

Abstract—In this paper the results of 67 soil sample investigations are presented. The spectral brightness coefficients were measured in the direction perpendicular to the surface of the samples. The linear and quadratic coefficients of the wavelength dependence are shown. The effect of different soil ingredients, humidity and roughness are analysed. The final purpose of this work is the application of these measured characteristics when using of data remotely sensed by satellites.

Key-words: reflection spectrum, albedo, soil ingredients, humidity, roughness.

1. Introduction

A part of solar irradiation is reflected by the surface and is spectrally transformed according to its material structural characteristics. The reflected portion and spectral transformation are characteristic of the surface and they are determined by its material composition, structure and condition. Meteorological investigations so far have mainly been restricted to the relationship between the reflection ratio and surface conditions. Material composition can only be deduced by the spectral resolution of the albedo. The spectral composition and dynamics of reflected radiation are very significant for both meteorology and the interpretation of information supplied by remote sensing. The spectral composition of the albedo provides information on the radiation energy utilised by the surface. Investigations in this area involve the technical-methodological development of detection, the reflection characteristics of representative surfaces and their interpretations.

2. *Methods and instruments used in investigations*

The reflection can be characterised by different parameters (see *Fig. 1*). In our investigations the brightness coefficient was determined. The measurement results serve as basis for the albedo definition.

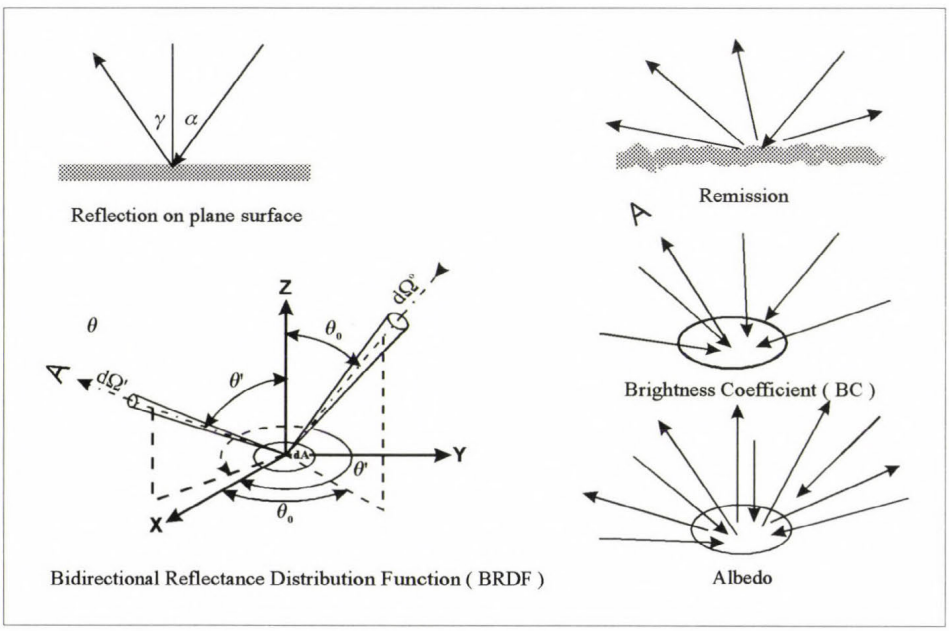

Fig. 1. The types of radiation reflection on surfaces of differing roughness.

Brightness coefficient

In field measurements, in most cases, it is impossible to illuminate the target surface from one direction only, this is why reasonable to introduce the brightness coefficient. The brightness coefficient is the ratio of the radiation energy scattered from δA surface at unit solid angle of θ', Φ' direction to the radiation energy arriving at the surface from total 2π solid angle.

Brightness coefficient mainly depends on the location of the detector as compared to δA surface (θ', Φ'). This does not mean, though, that the same surface examined from the same direction will produce constant values. It will be significantly affected by the distribution formula of the radiation R (θ_0, Φ_0) arriving at the surface.

The albedo

It is the ratio of the radiation energy scattered from δA surface at total 2π solid angle to the radiation energy arriving at the surface from total 2π solid

angle. The albedo can be taken as the weighted average of the brightness coefficientes (*BC*)

$$A = \int_0^{2\pi} BC(\theta', \Phi') \cos\theta' \, d\Omega'.$$

Weighting is necessary because, examined from θ' direction, δA surface will only mean $\delta A \times \cos\theta'$ surface. When calculating the albedo, the zenith point brightness coefficient ($\theta' = 0$, $\cos\theta' = 1$) counts for the most, therefore the brightness coefficient and the albedo concepts cannot be considered as synonymous. This is especially true, when the indicatrix is significantly distorted. Unfortunately, remote sensing-meteorological technical literature very often fails to distinguish between the two values.

In meteorological terminology the concept of albedo is used. Remote sensing detects radiation scattered and reflected at nearly nadir point, consequently, this value does not equal to the albedo.

To produce representative spectra the own-designed SM-1 and SM-2 reflection spectrophotometers, manufactured by LABOR-MIM, were used. The SM-1 and SM-2 are surface devices capable of determining continual spectra of the upgoing radiation reflected by soils and vegetation.

The measurement range of the SM-1 field reflection spectrophotometer is 400–1000 nm.

Major characteristics

- *Opening angle*: 7°, optical grid density: 1200 c/mm, detector: PIn photodiode, reflection standard: Ba SO_4, resolving capacity: 1 nm. The SM-2 is nearly a similar variety, the difference being its two-unit optical system.
- *Visual unit* (VIS): 400-1000 nm, infrared unit (IR): 1000-2400 nm. Characteristics: grid density VIS: 1200 v/mm, IR = 600 v/mm; detector VIS: PIn/Si photodiode, IR: PbS, photoresistor cooled to –38°. Reflection standard VIS: $BaSO_4$, IR: a diffuse surface coated with gold. Control and digital sign processing is carried out by the INTEL 8085 microprocessor.

After the calibration of the spectrometers, the measurement results were compared with internationally used measuring systems. When choosing the ranges, the operative ranges of about 50 spectrometers – produced in different countries – (LICOR, EXOTECH, BARNES) were considered.

The determination of different spectra was carried out in specifically built "black laboratories", using Tungsram sources of light. The dried samples were on a table in horizontal position and they were illuminated by several lamps. The spectrophotometer looked down at the investigated sample, so we actually measured the vertical brightness coefficient in each case.

The examined soil samples were taken in different regions of the country. The number of samples involved in the investigations is 67, their major physical and chemical characteristics were established by laboratory analyses. Thirty six of the samples were provided by the Soil and Agrometeorological Research Institute of the Hungarian Academy of Science, the clay samples were supplied by the Department of Soil Science of Gödöllő Agricultural University. For each measuring ground soil samples were used, providing reliable grounds for comparison making.

3. Measurement

Below the summary of findings follows that can be considered as significant. The results achieved give possibilities of international comparisons.

3.1 The reflection spectrum of soils

The investigations of the reflection spectra of soils were restricted to the analysis of macrophysical characteristics and the effects of soil condition. The representative soil spectrum refers to airdry, ground conditions.

The primary question is: what is the correlation (r) between the characteristic reflection and the wavelength for the Hungarian soils? The analysis of dried and powdered samples shows that the reflection increases as the wavelength grows. In the case of linear fitting, the slope is 0.015–0.041 in the 400–1000 nm interval.

In the range of 400–1000 nm the average reflection of soils in Hungary is

$$R_n(\lambda) = -5.278 + 0.022\,\lambda\,; \quad r = 0.986\,.$$

$R_n(\lambda)$ is the relative value of reflection referred to the wavelength (λ, nm). The high value of correlation coefficient suggests that soil reflection in the referred range is nearly linear. The higher the clay content of the soil is ($\Phi < 0.002$ mm) the stronger the linearity becomes. *Fig. 2* shows the reflection spectra of airdry sandy, loam and clay soils. It supports the view that soil texture has a decisive effect on reflectivity, which is most marked in the range of 500–1000 nm. Parabola can be better fitted to the measurements: r=0.985–0.999. The average quadratic coefficient is $-4.8 \cdot 10^{-5}$ for sandy soils (clay content $<10\%$); and $-2 \cdot 10^{-5}$ for clayey soils (clay content $>40\%$, mass ratio of sand 20%). The final conclusion on basic physical soil types can be described as follows

$$\begin{aligned}
\text{sand:}\quad & R_H\ \%\ (\lambda) = -5.4 \cdot 10^{-5} \times \lambda^2 + 0.124 \times \lambda - 37.1,\\
\text{loam:}\quad & R_V\ \%\ (\lambda) = -3.5 \cdot 10^{-5} \times \lambda^2 + 0.091 \times \lambda - 27.6,\\
\text{clay :}\quad & R_A\ \%\ (\lambda) = -0.6 \cdot 10^{-5} \times \lambda^2 + 0.036 \times \lambda - 11.3,
\end{aligned}$$

where λ is the wavelength. The reflection spectrum of different soils can be

described in different ways, by different parameters. The characteristic parameters used in the measurements are

- reflection in 400 nm,
- slope in the *range* of 400–1000 nm (direction tangent),
- the precision of linear trend fitting,
- the precision of quadratic trend fitting.

The reflection values at 400 nm are significantly different for major physical soil types: sand=3.7–4.6%, loam=2.8–3.5%, clay=1.9–2.6%. The 400 nm reflection value can be considered as a deterministic parameter as it conse-

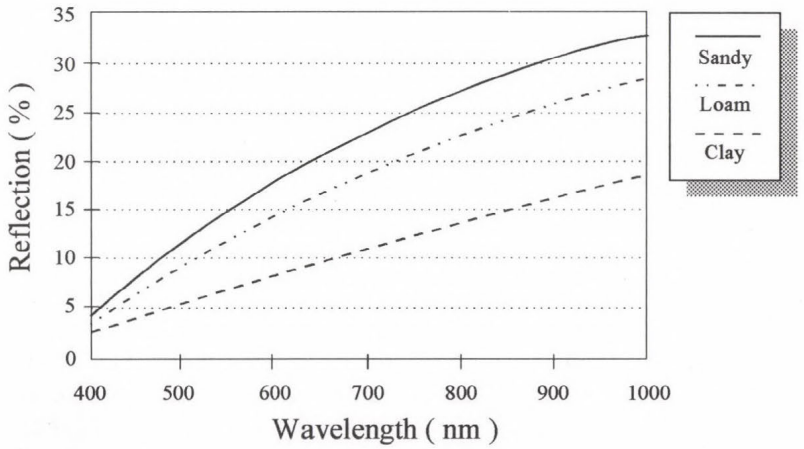

Fig. 2. The spectral reflection of different soils.

quently changes with the clay content ratio. The band 400–1000 nm is the most significant range of the solar spectrum. The lowest reflection value was measured at about 400 nm. Maximum soil reflection was measured in the range of 1200–1300 nm which supports *Baumgardner et al.*'s (1985) findings. The investigations show that the lower the clay fraction ratio, the steeper the referred range of the spectrum. According to the analyses of some 80 soil varieties collected in Hungary, the steepness of reflection spectrum in sandy soils is 3.0%/100 nm, it is 1.5%/100 nm in loam and it is as low as 1.0%/100 nm for clay. This allows to determine the physical type of the soil by its reflexion spectrum.

A linear equation can very well be fit to the referred range of the reflection spectrum. For the examined soils the fit is between r=0.92–0.99 (n=36). For parabolic equations r=0.95–0.99.

This regularity can be used for the categorization of undefined soils. Let's take the definite integral (D_i)

$$D_i = \frac{1}{1000 - 400} \int_{400}^{1000} (Rx\,(\lambda)) - (Ri\,(\lambda))\, d\lambda,$$

where $Rx(\lambda)$ is the spectral reflectivity of the unknown, $Ri(\lambda)$ is the spectral reflectivity of the known soil sample. The smaller the difference will become, the more similar the undefined characteristics is to the known soil type. It was found that, in 70% of the cases, this classification gives the same result as the classification made by granule composition definition. The method can be further developed if the number of the known soil categories is increased.

2.2 The effect of soil ingredients on the reflection spectrum

Soil ingredients are minerals and organic matters produced by different chemical processes. About 95% of materials of mineral origin derive from sedimentary rocks. The mineral ingredients of the soil are oxides, silicates, phosphates, sulphates, carbonates and chlorides (*Di Gleria et al.*, 1957). These materials are present in the form of compounds of different crystal structures. They differ in colour, and so, they have different optical characteristics. Below, some of the spectrometric characteristics of soil ingredients will be discussed. The results refer to airdry conditions.

Humus

It is the most important component of fertile soil, its volume percentage varies between 1–7%. As humus content increases, reflection decreases. Turf is the richest in humus, its reflection being the lowest. This soil nears black body both in the visual and infrared ranges ($R<7\%$).

Clay minerals

They are very important building blocks of the soil, effecting soil nutrient and water management (*Stefanovits*, 1981). The following clay minerals were examined: kaolinite, montmorillonite, illite; they are of fairly different crystal structure, their attitudes to water also differ. They belong to silicates mainly, which is of importance in thermoemission. They do not differ significantly in the visual range, but marked differences (as the effect of hydroxile residue) can be found in the infrared range (*Csákiné Michéli*, 1991). Reflection decrease is the strongest in the montmorillonite (27%), it is weaker in the kaolinite (18%). No difference can be found in the range of the second hydroxile residue (*Figs. 3a, 3b, 3c*).

Soil ingredients represent different volume percentages in the soil which, in turn, affects reflection (*Fig. 4*).

Ferric oxide (Fe_2O_3)

Ferric oxide affects the reflecting capacity of the soil fairly significantly. As it is known, Fe_2O_3 and Fe_3O_4 have very different reflecting characteristics. The reflecting capacity of Fe_3O_4 is constant in the examined range, whereas that of Fe_2O_3 depends on the wavelength. The dominant feature in the 650–760 nm red

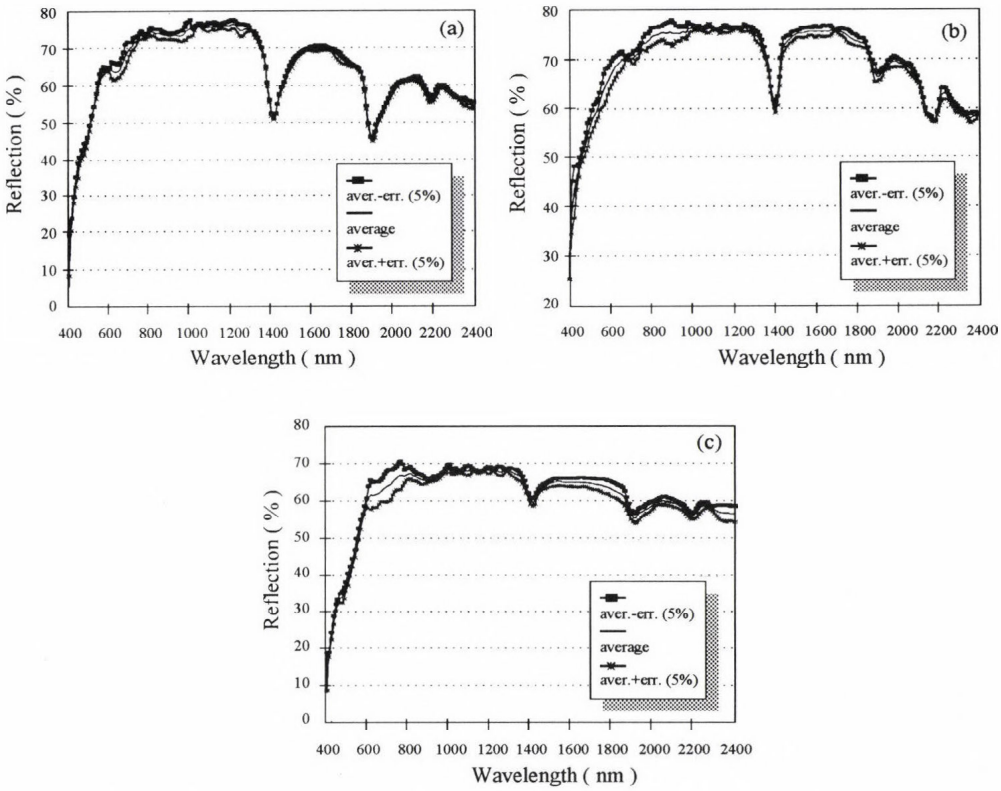

Fig. 3. The spectral reflection of montmorillonite *(a)*, caolinite *(b)* and illite *(c)*.

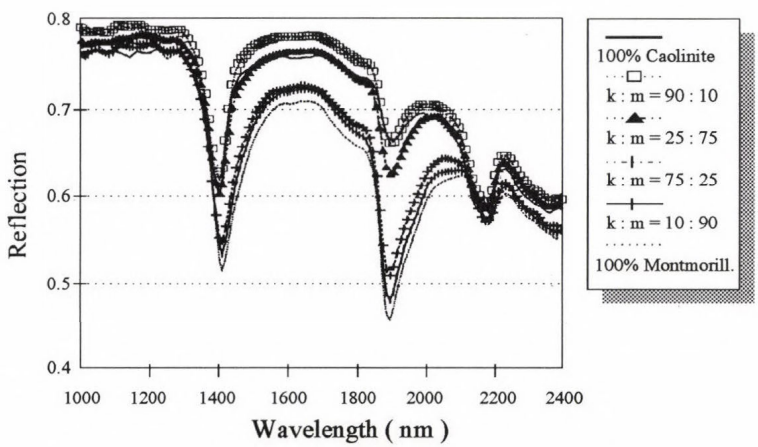

Fig. 4. The spectral reflection of the mixture of montmorrillonite and caolinite of different mass proportions.

range is the reflection, in the 450–500 nm blue range it is the absorption.

Airdry soils contain Fe_2O_3 mainly, and, so, spectral characteristics can be used for the quantitative definition of iron in the soil. The significant differences that exist between the reflection of different physical soil types should not be ignored though, as they may cover up the effect of ferric oxide. Consequently, no relationship generally applicable for all soil types can be established between reflection and Fe_2O_3 content.

Ferric oxid in loom

The majority of the examined samples was loam, so the conclusions below will refer to this soil type. For quantitative determination *Obuhov* and *Orlov* (1964) suggest the $C\% = 17.35 - 0.20\ R\%$ (640) relation between Fe_2O_3 content (C) the reflection value (R) in the 640 nm range. This relation was not proven by our investigations.

A new reflection parameter was introduced in the evaluation process, a *NRB* (normalized red-blue) index, which is defined as follows

$$NRB = \frac{R\%\,(710) - R\%\,(480)}{R\%\,(710) + R\%\,(480)}.$$

$R\%$ (710) is the reflection in 710 nm, $R\%$ (480) is the refleciton in 480 nm. In the samples this index varies between 0.25–0.5 and shows a strong relationship to the iron content of the soils. The equation used for the determination of $C\%$ (Fe_2O_3 content) is this

$$C\% = 1.09 + 11.5\ NRB\ (R = 0.75).$$

It should not be forgotten that this equation refers to loam soils only, where the iron content determined with X-ray fluorescent method is 2–5%. To establish similar relationship for sandy and clay soils is a task to be solved in future.

Soil humidity

It is the soil humidity that can modify the reflection spectrum most strongly. Soils hold their water contents against gravity with the help of capillary and sorption forces. Basically, the reflection effect of water content is expressed by the relationship between clay fraction and spectrum characteristics. The spectral charasteristics effected by humidity are:

- the measure of linearity,
- the R_{400}/R_{1000} quotient, slope,
- the R_{400} value,
- hydrate-adsorption in NIR.

Linearity has already been discussed, now it has to be added that it is increased by the growth of water content. The R_{400}/R_{1000} quotient is a specific parameter. In clay soils (clay fraction >60%) the slope is not significantly

increased by raised water content. The slope changes slightly in loam, but sharply in sand. Consequently, the angle of dry and wet spectra curve serves as a soil type specific parameter (*Fig. 5*).

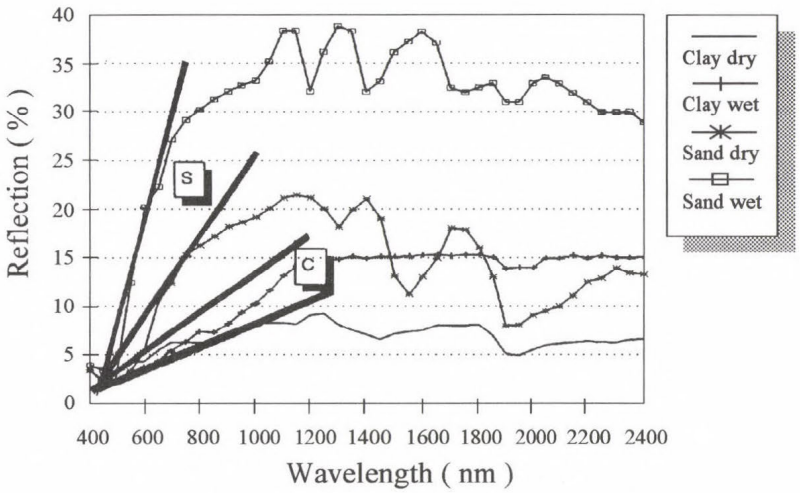

Fig. 5. The spectral reflection of dry and wet sand and clay soils.

Soil roughness

Natural soils, and even laboratory soil samples have more or less rough surfaces. (Even pressed soils are considered rough. This can easily be detected with a simple magnifying glass.)

If the reflections of a relatively smooth surface and those of its roughened variety are compared, the conclusion is that the size of reflection decreases as roughness increases. This can be explained with the following two simple models

(a) Mirroring reflecting surface

Supposing that plane surfaces totally reflect incoming light, according to the law of reflection, radiation will be detected in one direction only. If the rough surface is modelled by triangles, radiation will be detected in several directions, supposing again total reflection from the sides of the triangles.

(b) Lambert surface

The radiation of the real Lambert surface is constant, whichever direction is considered

$$L(\theta, \Phi) = a/\pi \; L_0 \sin\alpha ,$$

where L is the irradiation, a is the albedo of the surface, α is the angle of irradiation, L_0 is the radiation of the source of light.

This means that the *BRDF* (see Fig. 1) of the Lambert-type surface is independent of the direction of lighting and observation, it only depends on the albedo of the surface

$$BRDF\ (\text{Lambert}) = a/\pi.$$

If the rough surface is modelled by triangles whose sides are supposed to be Lambert-type reflecting surfaces , and the irradiation of the surface elements by each other is neglected (this factor is of importance only for bright surfaces—R nears one—and by high β values), the radiation of the surface can be defined in the following way (*Fig. 6*)

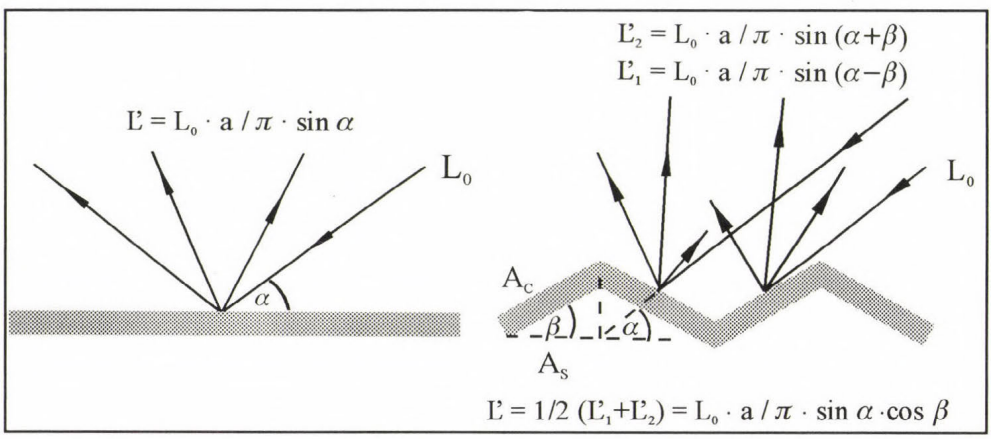

Fig. 6. The diffuse reflection of plane and rough surfaces.

$$L(\theta, \Phi) = R/\pi\ L_0\ \sin\alpha\ \cos\beta;$$

the *BRDF* of rough surfaces, consequently, is

$$BRDF(\text{rough}) = a/\pi\ \cos\beta.$$

If the result is compared with the *BRDF* of plane Lambert surface

$$BRDF(\text{rough}) = BRDF(\text{Lambert})\ \cos\beta.$$

According to Fig. 6 $\cos\beta$ is

$$\cos\beta = A_s(\text{plane})/A_c(\text{rough}),$$

the converse of unit rough surface per unit plane surface. This value is considered as the roughness characteristic.

A rough surface can be taken as a random distribution of elementary plane surfaces (mirroring and Lambert-type), which explains reflection decrease against the increase in roughness.

This method can be improved if soil granules are modelled with spheres. A very reliable model was elaborated by *Cierniewski* (1987), in which soils are modelled by spheres placed on directed surface. Unit sphere surface per unit surface seen from above is taken as roughness factor. The distance between the centres of the spheres is larger than their diameters, and so their reciprocal shading effect, which produces ellipses in this case, has also to be taken into consideration.

A practicable method was also elaborated by *Bunnik* (1987), in whose SOIL model soil surface is modelled by cylinders placed on a horizontal surface. The advantage of this method is its suitability to model for example the reflection of forests by enlarging sizes.

Investigations were made into the question whether roughness modifies the spectral composition of reflected radiation. It was established that roughness decreases reflection in all ranges, but no spectral differences were found.

A further question is whether there are differences between the reflections of parallely and perpendicularly lit surfaces if furrows are cut into the soil samples. This simple modelling was designed to explain the relationship between furrow direction and reflection. (A similar question arises when the effect of the row direction of grown plants on reflection is investigated.) It was found that furrows perpendicular to lighting direction significantly reduce reflection. (This, of course, means radiation reflected into zenith point. Furrows perpendicular to lighting backscatter considerably higher than those parallel to lighting.)

If lighting is homogeneous and the sample is turned around, no statistically provable differences were detected.

4. Discussion of research results

As a conclusion, it can be established that the vertical brightness coefficient measured under equal geometrical conditions expresses several material characteristics of the surface and is strongly modified by the changes in the conditions. This value transformed to π solid angle will give the albedo. Yet, it has to be noted that this value is the *homogeneous albedo*. Obviously, no such homogeneous surface exists in reality, and so, the calculated value will only approximate the conventionally measured albedo.

(1) The albedo of rough surface can be determined as the weighted sum of the measured *BC* values (brightness coefficient). Weighting is made by the cosinus of the angle of observation (θ') by this integral

$$a_r = \int_0^{\pi/2} BC(\theta') \cos\theta' \sin\theta' \, d\theta'.$$

If soil reflection is perfectly Lambert-type, *BC* would give a constant value

independent of direction, and so

$$a_L = \pi\ BC$$

that is, the albedo can be calculated if plumb point *BC* is known.

(2) Soil reflection cannot be considered Lambert-type, not even approximately. The greater the deviation of the soil from the ideal diffuse reflection surface, the more the deviation of the albedo calculated from the actual one. The relation between the two albedoes is characteristic of the soil and is affected mainly by roughness, consequently, it can be considered as the optical roughness parameter (*ORP*)

$$ORP = a_r/a_L = a_r/\pi\ BC.$$

a_r is the albedo of the rough and a_L is that of the Lambert surface. If the roughness parameter is known, the albedo of the surface can be determined by measuring the plumb point *BC*.

(3) The radiation arriving at a given plane and reflected to the total hemisphere, and also the proportion between them, can be measured with pyranometers. This measurement involves the effect of the roughness and the deviation from the Lambert surface. The magnitude of the two effects is

$$\triangle a = a_L - a_m,$$

a_m is the measured albedo value. The smaller the $\triangle a$, the smaller the degree of the roughness of the surface.

The conclusions made above support the view that the spectral analysis of reflection supplies plenty of practical information to increase the efficiency of interpretation.

Acknowledgements—Authors are grateful to *Academician G. Várallyay* director of the Department of Soil and Agrochemical Research Institute of Hungarian Academy of Science and to *Academician P. Stefanovits*, for their contribution with soil samples and clay minerals for the measurements.

This work has been supported by *Hungarian Academy of Sciences* as an OTKA project, contract number: 1173.

References

Baumgardner, M.F., Silva, L.F., Biehl, L.L. and *Stoner, E.R.*, 1985: Reflectance properties of soils. *Adv. Agron. 38*, 1-44.

Bunnik, N.J.J., 1987: The multispectral reflectance of shortwave radiation by agricultural crops in relation with their morphological and optical properties. Mededelingen Lnadbouwhogescholl, Wageningen, The Netherlands, 78-100.

Cierniewski, J., 1987: A model for soil surface roughness influence on the spectral response of bare soil in the visible and near infrared range. *Remote Sens. Environ. 23*, 97-115.

Csákiné Michéli, Erika, 1991: *The Complex Optical Reflectance of Artificial Mineral Humus* (in Hungarian). Ph. D. Thesis. Agricultural University, Gödöllő, Hungary.

Di Gleria, J., Klimes-Szmik, A. and *Dvoracsek, M.*, 1951: *Soil Physics and Soil Colloids* (in Hungarian). Akadémiai Kiadó, Budapest.

Obuhov, A.E. and *Orlov, D.S.*, 1964: Spectral reflectivity of major soil groups and possibility of using diffuse reflections in soil investigations (in Russian). *Soviet Soil Science 1*, 174-184.

Stefanovits, P., 1981: *Soil Science* (in Hungarian). Mezőgazdasági Kiadó, Budapest.

Szász G., 1987: The importance of agricultural remote sensing in agrometeorology (in Hungarian). *Időjárás 91*, 88-103.

IDŐJÁRÁS

Quarterly Journal of the Hungarian Meteorological Service
Vol. 98, No. 1, January–March 1994

Validation of crop simulation model CERES-Maize

M. Hunkár

Agrometeorological Research Station,
P.O. Box 80, H-8361 Keszthely, Hungary

(Manuscript received 14 January 1994; in final form 3 March 1994)

Abstract—A crop simulation model must first be capable of representing the actual performance of crops grown in any particular region before it can be applied to the prediction of agrotechnology or climate change impacts. CERES-Maize model was developed by the United States Department of Agriculture, Agricultural Research Service (USDA-ARS). The model is designed to simulate the effects of cultivar, planting density, weather, soil moisture and nitrogen on crop growth, development and yield. Version 2.1 was used in the present study. Crop analysis of maize was carried out at the Agrometeorological Research Station at Keszthely, Hungary in the years 1976-1991. Measured and simulated data of silking date, maturity date, leaf area maximum, final biomass and grain yield were compared. The average differences between the predicted and observed plant characteristics are not more than 4%. The probability, that of CERES-Maize model simulated yield and biomass agreed within 15% with observed values in a given year, is 80%. A summarized index-value was developed with a scale ranging from 0 to 5. On the basis of 16 years simulation experiments the index-value of CERES-Maize model was 4.23.

Key-words: maize, simulation model, CERES-Maize, validation.

1. Introduction

"Simulation may aid the understanding of important aspects of complex systems in such a way that their behaviour is visualized and a guide to their management is obtained. But solutions are only accepted as such methods to falsify them are available, if they can be verified or their usefulness can be proven" (*Rosenberg et al.*, 1992). Several crop models are known in the literature and most of them is unique concerning their input requirements therefore the adaptation and validation of any models is not an easy task.

The International Benchmark Sites Network for Agrotechnology Transfer (IBSNAT) Project was established in 1982 in the USA (*IBSNAT*, 1990). The IBSNAT project was designed to provide the structure and mechanism to link soil, moisture conditions, weather, crop and management research efforts into

a coherent problem-solving procedure. In the first phase of the project twelve main food crops (maize, rice, sorghum, millet, barley, wheat, soybean, peanut, phaseolus bean, cassava, taro and potato) were identified for model development and simulation. These twelve food crops were divided into three groups on the basis of their similarity structure. The name of model families are CERES for grain crops, SOYGRO for legumes and SUBSTOR for storage plants. All of the models simulate daily incrementing and require daily weather data consisting of maximum and minimum air temperature, solar radiation and rainfall data as driving forces. Local conditions are described by standard soil characterization. Initial values of water content of the soil are also required. This relative simplicity in data requirement and the detailed documentation of the models make possible to run simulation experiments also for Hungarian conditions. In the present paper the evaluation of CERES-Maize model is given.

2. Material and method

2.1 The crop model

CERES-Maize model (*Jones* and *Kiniry*, 1986) is a multipurpose user-oriented simulation model. In order to accurately simulate maize growth, development and yield, the model takes into account the following processes:

- phenological development, especially as it is affected by genetics and weather,
- extension growth of leaves, stems and roots,
- biomass accumulation and partitioning, especially as phenological development affects the development and growth of vegetative and reproductive organs,
- soil water balance and water use by crop,
- soil nitrogen transformations, uptake by the crop, and partitioning among plant parts.

The model calculates crop phasic and morphological development using temperature data, daylength and genetic characteristics. Leaf expansion, growth and plant population provide information for determining the amount of light intercepted, which is assumed to be proportional to biomass production. The biomass is partitioned into various growing organs in the plant using a priority system. A water and nitrogen balance submodel provides feedback that influences the development of growth processes. These are multilayer models. The number and depth of the layers are optional but it is suggested to reach the depth of root system. There is a possibility to switch off the water and nitrogen submodels which means that the nutrition shortage or water shortage is avoided using fertilizer and irrigation on optimum level. In this case the light and temperature conditions form the potential production.

Crop cultivars differ one from another in a whole array of morphological

and other characteristics. The "genetic coefficients" that summarize the way in which a specific crop cultivar divides up its life cycle, respond to different aspects of its environment, or appear changes morphologically. The number of potential genetic coefficients is very large. However, the general aspects of adaptation to any given environment are determined by a few responses, and these have been taken into account in the current models. For maize there are five coefficients. Three are related to the development and progression through the life cycle, while two are related to growth aspects. To choose appropriate genetic coefficients is a crucial process in model adaptation. The model documentation contains the values of genetic coefficients for about 50 varieties of maize.

2.2 Field experiments

Biomass production, leaf area index and grain yield of maize were measured together with phenological observations at the experimental field of the Agrometeorological Research Station of the Hungarian Meteorological Service at Keszthely in the years 1976–1991. The size of the experimental plot is 900 m^2. Sowing density was 70,000 plants/ha. Sowing depth was 5 cm. The soil is a Ramman type brown forest soil, its characteristics are shown in *Table 1*. Only

Table 1. Soil characteristics of Ramman brown forest soil at Keszthely

Layer mm	Wilting point cm^3/cm^3	Field capacity cm^3/cm^3	Saturation moisture content cm^3/cm^3	Moist bulk density g/cm^3
0 - 5	0.070	0.29	0.46	1.71
5 - 15	0.081	0.32	0.45	1.78
15 - 30	0.095	0.35	0.40	1.96
30 - 40	0.091	0.32	0.45	1.79
40 - 50	0.071	0.35	0.45	1.79
50 - 60	0.091	0.33	0.46	1.79
60 - 70	0.091	0.36	0.44	1.79
70 - 90	0.061	0.38	0.43	1.88
90 -120	0.085	0.36	0.39	2.02
120 -150	0.085	0.36	0.39	2.02

one maize variety was grown in each year but it altered several times during this 16 years period. Maize variety SZTC-255 was used in 9 years, Pioneer 45 3901 in three years, Pioneer 3782 in two years, Pioneer 3978 and KSC-360 in one year. The level of nitrogen fertilization was the same in each year, 200

kgN/ha. This amount can be taken to be optimum. There was no irrigation, the plot was rainfed in each year. Initial soil moisture content was measured at the time of sowing by thermo-gravimetric method. Leaf area index (LAI) and the dry weight of above ground biomass were measured several times during the vegetation period using sample plants. In the present study the maximum leaf area index which occurs at the time of silking, and the final amounts of above ground dry biomass and grain yield containing 15% moisture were used.

The daily meteorological data as minimum and maximum air temperature, global radiation and precipitation amount were measured in a standard way next to the experimental field.

2.3 Simulation experiments

The first step in the model adaptation is to choose or determine the genetic coefficients of the given cultivar. In our case the genetic coefficients had to be estimated on the basis of phenological observations. The applied genetic coefficients are shown in *Table 2*. The meanings of denotations are as follows:

- *P1* – growing degree days base 8°C from seedling emergence to the end of the juvenile phase,
- *P2* – photoperiod sensitivity coefficient. Juvenile phase and photoperiodic sensitivity are uncommon in the routine observation system. They were measured for a number of cultivars grown in controlled environments by *Kiniry et al.* (1983a, b). For other cultivars they can be estimated,
- *P5* – growing degree days base 8°C from silking to physiological maturity,
- *G2* – potential kernel number per plant,
- *G3* – potential kernel growth rate in mg/kernel day.

Table 2. Genetic coefficients applied in simulation experiments for the different cultivars of maize

Cultivar	Genetic coefficients				
	P1	P2	P5	G2	G3
SZTC-255	110	0.1	700	780	8.6
PIO 3901	140	0.1	720	600	9.0
PIO 3782	200	0.7	800	650	8.5
PIO 3978	110	0.1	720	700	10.0
KSC-360	165	0.0	600	760	9.6

Because of the lack of the measurements of nitrogen concentration in the soil and in the plant, the nitrogen submodel was switched off. It may not cause too

much error because the amount of applied nitrogen fertilizer – 200 kg N/ha – can be taken to be optimum as it was shown by *Dávid* (1981).

Simulation experiments were carried out for 16 years using the actual weather data, cultivars, sowing depth and density, and initial soil moisture content.

3. Results and discussion

From the model outputs the date of silking and maturity, the final amounts of biomass, the grain yield and the maximum leaf area index were selected for comparing them with observed data.

Before the year by year analysis let's see the differences in the averages. *Table 3* shows a very good agreement between the predicted and observed average values in the 16 years. The differences in silking date are only 0.2 days, in maturity date 3.3 days, in LAI max 0.01, in grain yield 386 kg/ha, in dry biomass 375 kg/ha. Also the standard deviations of the simulated and observed values are well correlated. This extremely good agreement in the averages means that the CERES-Maize works at least as good as a statistical model. The estimation of the effect of weather for longer period gives reliable results.

Table 3. Averages (av) and standard deviations (sd) of predicted and observed plant characteristics

	Predicted		Observed	
	av	sd	av	sd
Silking date (day of the year)	199.7	8.3	199.5	8.0
Maturity date (day of the year)	260.4	14.6	257.0	14.2
Biomass (kg/ha)	17,716	2,552	18,091	3,124
Grain yield (kg/ha)	10,681	2,190	10,294	2,008
LAI max (m^2/m^2)	3.42	0.64	3.43	0.59

Fig. 1 shows the differences in silking date year by year and the differences between the observed and predicted maturity date. According to the silking date there is no systematic error in the prediction. In most of the years the predicted maturity date occurs later than it was observed. The cumulated distribution of the error of the prediction for these phenological stages are shown in *Fig. 2*. The length of the phenological phase from silking to maturity is influenced by the genetic coefficient *P5*. If we choose smaller value for growing degree days the length of this phase will be shorter. But if this period is shorter the biomass production will be less. It would result improvement only in 50% of the years, in the rest of the years the biomass prediction would be worse and also the grain yield would be less which is not required as it is shown in *Fig. 3*. Since

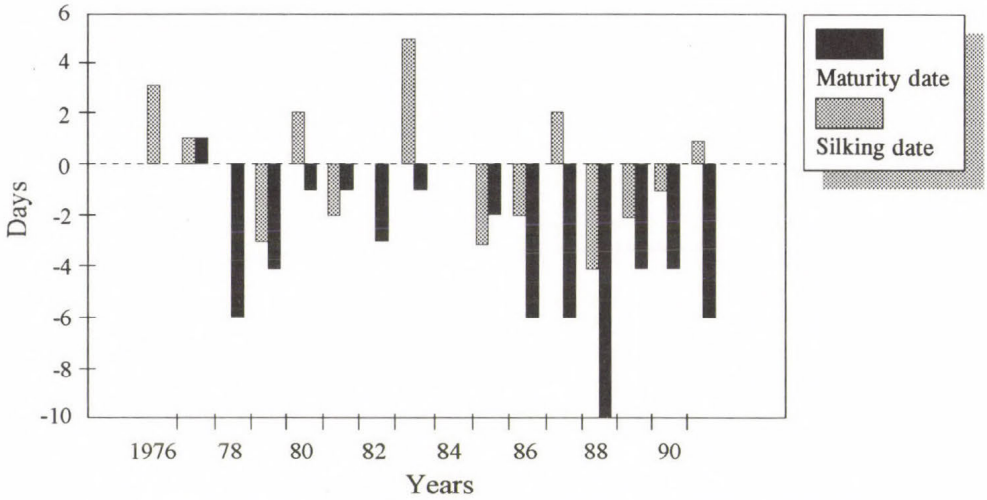

Fig. 1. Differences in silking date and maturity date: observed − predicted.

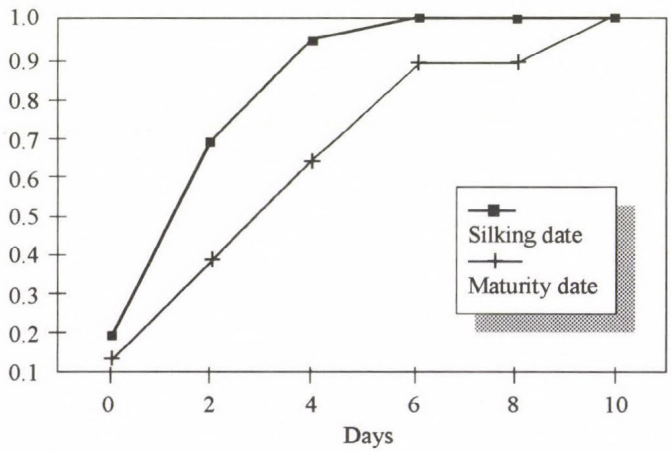

Fig. 2. Cumulative error of model prediction for silking date and maturity date.

the grain yield is the most important output from economical viewpoint in *Fig. 4* also its absolute values are presented year by year. *Fig. 5* shows the cumulative error in percentage for the final amount of biomass and grain yield. The probability, that the differences between the predicted and observed biomass and grain yield are not more than 15%, is at least 80%. The prediction of maximum leaf area can be judged reliable. The differences between the observed and predicted values were larger than one only in 1983 as it can be seen in Fig. 3. The cumulative error for the leaf area maximum can be seen in Fig. 5.

Besides the evaluation of the individual model outputs an index-value was

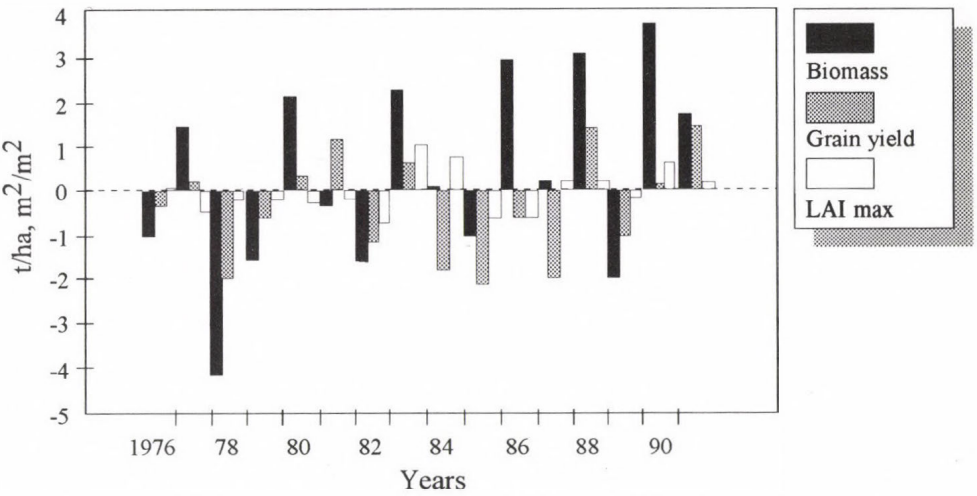

Fig. 3. Differences in the final above ground biomass (t/ha), grain yield (t/ha) and maximum leaf area index (m^2/m^2): observed − predicted.

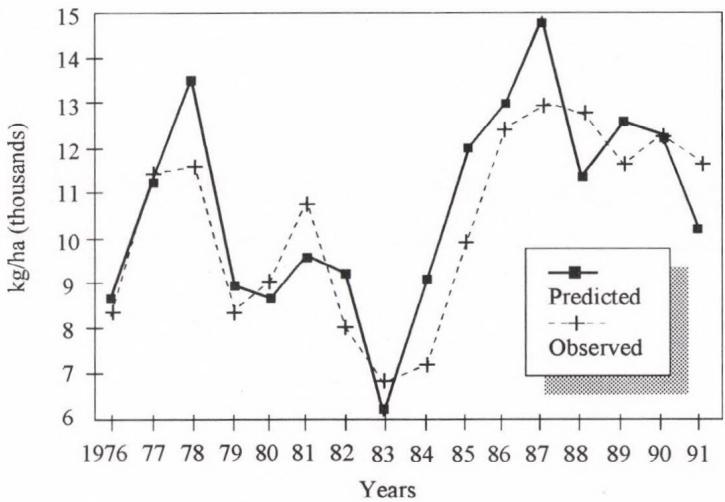

Fig. 4. Predicted and observed grain yield year by year.

created to assess the skilfullness of the model. Considering the differences between the observed and predicted values a more or less arbitrary scale is given for the evaluation. In *Table 4* the skill-score of prediction is presented for the individual outputs. When the predicted value shows a very good agreement with the observed value this output gets 1 point. If the agreement is not so good the output gets a point of less than 1 while a very bad agreement is characterized with 0 point.

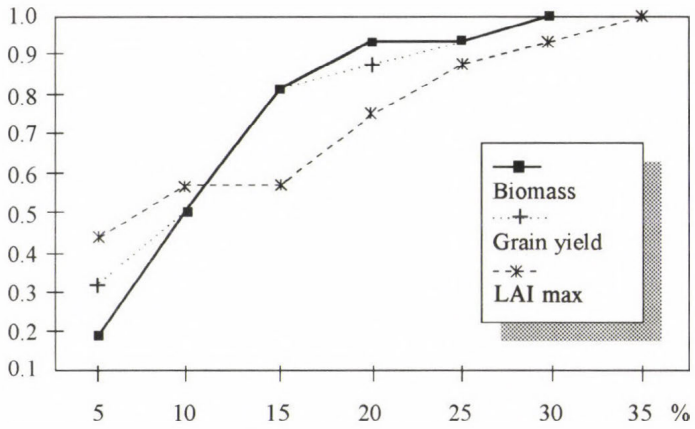

Fig. 5. Cumulative error of model prediction for grain yield, biomass production and maximum leaf area index.

Summing up these points for the five outputs we get an index-value between 0 and 5. In *Table 5* the skill-score of the individual outputs and the index-values of the whole model prediction are presented for each year. In 13 years the index-value is greater than or equal to 4, and its smallest value is 3.5.

Table 4. Scale of skill-scores of prediction

Deviation ± Days	Deviation %	Skill-scores
2	< 5	1.0
3	5 - 10	0.9
4	10 - 15	0.8
5	15 - 20	0.7
6	20 - 25	0.6
7	25 - 30	0.5
8	30 - 35	0.4
9	35 - 40	0.3
10	40 - 45	0.2
11	45 - 50	0.1
> 12	> 50	0.0

4. Conclusions

CERES-Maize model is a comprehensive method for describing growth and development of maize plant. Since the documentation and dissemination of the

Table 5. Skill-scores of model outputs and the index-value for each year

Years	Skill-scores					Index value
	Silking date	Maturity date	Grain yield	Biomass	LAI max	
1976	0.9	1.0	1.0	0.9	1.0	4.8
1977	1.0	1.0	1.0	0.9	0.6	4.5
1978	1.0	0.6	0.7	0.5	1.0	3.8
1979	0.9	0.8	0.9	0.8	1.0	4.4
1980	1.0	1.0	1.0	0.8	0.9	4.7
1981	1.0	1.0	0.8	1.0	1.0	4.8
1982	1.0	0.9	0.8	0.8	0.6	4.1
1983	0.7	1.0	0.9	0.7	0.4	3.7
1984	1.0	1.0	0.5	1.0	0.5	4.0
1985	0.9	1.0	0.6	0.9	0.6	4.0
1986	1.0	0.6	1.0	0.8	0.7	4.1
1987	1.0	0.6	0.7	1.0	1.0	4.3
1988	0.8	0.2	0.8	0.8	0.9	3.5
1989	1.0	0.8	0.9	0.8	1.0	4.5
1990	1.0	0.8	1.0	0.7	0.7	4.2
1991	1.0	0.6	0.8	0.9	1.0	4.3
Averages	0.95	0.81	0.84	0.83	0.81	4.23

model is well organized, the model is well known in a wide area of the world. The effects of meteorological elements are taken into account in explanatory way, and for a longer period the average differences between the predicted and observed plant characteristics are not more than 4%. Considering the extent of this uncertainty the model is suitable for studying climate impact even by this 2.1 version which does not contain the direct effect of atmospheric CO_2 concentration. Recently the model developers have been working on a more sophisticated version for taking into account also the direct effect of the atmospheric CO_2 and other environmental effects including mineral nutrition other than nitrogen and pests as well. It makes possible in the future to study the plant responses to different environmental factors as a part of a whole system.

References

Dávid, A., 1981: Connection between weather, fertilization and characteristics of the development of maize (in Hungarian). *Időjárás 85*, 103-111.

IBSNAT, 1990: *Network Report 1987-1990*, IBSNAT PR., University of Hawaii.

Jones, C. A. and *Kiniry, J.R.* (eds.), 1986: *CERES-Maize A Simulation Model of Maize Growth and Development*. Texas A&M University Press, College Station.

Kiniry, J.R., Ritchie, J.T. and *Musser, R.L.*, 1983a: Dynamic nature of the photoperiod response in maize. *Agron. J. 75*, 700-703.

Kiniry, J.R., Ritchie, J.T., Musser, R.L., Flint, E.P. and *Iwig, W.C.*, 1983b: The photoperiod sensitive interval in maize. *Agron. J. 75*, 687-690.

Rosenberg, N.J., McKenney, M.S., Easterling, W.E. and *Lemon, K.M.*, 1992: Validation of EPIC model simulations of crop responses to current climate and CO_2 conditions: comparisons with census, expert judgement and experimental plot data. *Agricult. Forest Meteorol. 59*, 35-51.

IDŐJÁRÁS

Quarterly Journal of the Hungarian Meteorological Service
Vol. 98, No. 1, January–March 1994

Solar radiation components at Qena, Egypt

Sayed M. El Shazly

Department of Physics, Faculty of Science, Qena University
Qena, A.R. Egypt

(Manuscript received 28 December 1993; in final form 22 February 1994)

Abstract—A solar radiation station has been established in Qena, Upper Egypt. Measurements of hourly global and diffuse solar radiation on a horizontal surface for February and March 1992 have been used to derive formulas that predict the monthly mean of hourly global solar radiation including its diffuse and direct components. A statistical procedure has been developed to compute correlations between the daily global radiation and its diffuse component.

Key-words: solar radiation components, measurements empirical model, statistical correlations, Qena.

1. Introduction

Very precise measurements of different solar radiation components are required for solar energy users in order to design any solar energy system or study of the potential of solar energy in a region. Solar radiation data for most parts of the world are now available (*Lenung,* 1980). However, such information for developing countries is scarce.

Qena is located at the south part of Egypt (ϕ=26°10', λ=32°43', H=78 m asl). She is almost dry and free from clouds all year around, which makes of richly supplied with the available solar energy. The aim of this paper is to describe the station for measuring the global solar radiation and its diffuse component over Qena city, and to present an empirical model derived from the measured data to estimate different solar radiation components.

2. Measurements

Principally, there are three components of paramount importance in solar energy utilization, namely: global (G), diffuse (D) and direct (I) solar radiation.

These components are related to each other according to the following relation (*WMO*, 1983)

$$G = D + I \sin h, \tag{1}$$

where h is the solar elevation angle. In this work both G and D were measured, while I was calculated.

2.1 Measurements and instruments

The solar radiation was measured by two Kipp and Zonen precision pyranometers (Model CM 6B). This type of pyranometers is designed for measuring the irradiance on a plane surface, which consists of the direct and diffuse solar radiation incident from the hemisphere above, and complied with the specification for "first class" pyranometer (*WMO*, 1983). For measuring the diffuse component of solar radiation on the horizontal surface, the direct solar component was shielded semi automatically from one of the two pyranometers, by using shadow band constructed by the author following Kipp and Zonen rules. The band guarantees a stable stand even at high winds. The objective of the shadow band is to intercept the direct radiation of the Sun during the whole day. It intercepts not only the direct radiation but also a small part of the diffuse sky radiation, so the measured data were multiplied by a correction factor (*Latimer* and *Mac Dowall,* 1971) equal to

$$I/(I - F/D), \tag{2}$$

where

$$F/D = \frac{2\omega}{\pi\gamma} \cos^3\delta \, (\sin\phi \, \sin\delta \, H_0 + \cos\phi \, \cos\delta \, \sin H_0). \tag{3}$$

In Eq. (3) ω is the width of the shadow band, γ is its radius, δ is solar declination, ϕ is station latitude, H_0 is the hour angle of the Sun at sunset. For our station and shadow band design (ω=60 mm, γ=610 mm, ϕ=26.10°), the correction factor varies between 1 and 1.14 depending on the measurement date is applied. The setting of the shadow band was checked daily at 11.00 hr making sure of the centering of the Sun image on it. Every few days the band position is adjusted to the declination of the Sun. The pyranometers are securely mounted on steel stands located on the roof of the Faculty of Literature, Qena University (18 m above the ground), free from any obstruction above the plane of the sensing elements. The instruments are not in proximity to light-colored walls or other objects likely to reflect solar radiation on it and it is not exposed to artificial radiation sources.

2.2 Recording system

Two channels solar integrator (Kipp and Zonen, Model CC 12) in

conjunction with the used pyranometers measures the solar irradiance (in W m^{-2}) and calculates the irradiations over selectable periods: 10, 30 or 60 minutes as well as over 24 hr. After requested period (60 minutes), two irradiation values per channel (sub and accumulating totals) and time are available on built in cartridge printer. Along with the solar radiation measurements, all the usual meteorological parameters which include those of particular interest to solar applications, such as temperature, relative humidity, pressure, cloud cover are observed at the same site.

3. Results and discussion

3.1 Monthly mean hourly values

Monthly means of hourly values (expressed in W m^{-2}) are tabulated in *Tables 1* and *2* for February and March 1992 of global (G), diffuse (D) and direct (I) solar radiation as well as the maximum and the minimum values recorded during the hour. The tables include also the standard deviation of the hourly values with respect to its mean, which is a convenient measure of the normal variability of the observed components. It is clear from these tables that the standard deviation is larger, for the same hour in March than in February. This indicates that during March the variability of cloudiness is larger.

The variation of the $\bar{G}$, $\bar{D}$ and $\bar{I}$ with the actual time t, is shown in *Fig. 1*. The curves suggest that the following empirical relations may be written

$$\bar{G} = a_1 + b_1 t + c_1 t^2 , \tag{4}$$

$$\bar{D} = a_2 + b_2 t + c_2 t^2 , \tag{5}$$

$$\bar{I} = a_3 + b_3 t + c_3 t^2 , \tag{6}$$

where a, b and c are constants determined for February and March and given in *Table 3*. It is clear from the figures that a very good fit is obtained between the measured solar radiation data, especially the diffuse component, and their estimation models represented by Eqs. 4, 5 and 6.

3.2 Correlation between the daily global radiation and its diffuse component

For this type of correlation, the most common empirical equations are linear expressions, produced by *Page* (1964)

$$K = 1.00 - 1.13 K_T \tag{7}$$

or cubic ones, suggested by *Klein* (1977), using data from *Liu* and *Jordan* (1960)

Table 1. Monthly means of hourly solar radiation components (W m^{-2}), February 1992. Station: Faculty of Science in Qena

		Time											Total
		7–8	8–9	9–10	10–11	11–12	12–13	13–14	14–15	15–16	16–17	17–18	
Global	Mean	172.0	389.0	586.7	730.0	805.4	814.7	761.5	520.8	422.0	204.8	32.5	5439.4
	Max.	212.4	443.0	643.2	790.0	881.5	898.3	834.8	677.1	470.3	249.7	52.4	
	Min.	130.4	334.4	534.8	677.2	758.0	758.3	710.5	525.1	384.5	175.5	20.9	
	S.D.	23.1	29.4	30.5	31.7	42.1	37.3	33.8	90.8	33.1	19.9	8.6	
Diffuse	Mean	74.7	119.7	142.4	160.7	168.4	171.5	163.6	149.5	124.0	81.6	20.0	1376.1
	Max.	110.4	200.1	191.6	215.4	236.4	244.5	245.4	220.6	180.5	115.2	29.8	
	Min.	62.6	95.3	122.4	141.8	138.4	139.4	144.0	136.0	103.3	71.1	13.9	
	S.D.	13.2	24.2	16.5	20.9	25.4	28.9	29.3	26.3	18.0	11.0	5.2	
Direct	Mean	662	760	838	860	857	839	806	720	594	386	113	7435
	Max.	873	888	896	902	920	913	866	789	692	496	204	
	Min.	167	413	730	767	692	673	662	471	334	280	80	
	S.D.	144	95	38	38	65	63	58	79	83	56	30	

Table 2. Monthly means of hourly solar radiation components (W m^{-2}), March 1992. Station: Faculty of Science in Qena

		Time											Total
		7–8	8–9	9–10	10–11	11–12	12–13	13–14	14–15	15–16	16–17	17–18	
Global	Mean	225.0	480.3	684.3	811.5	886.5	886.3	824.3	678.9	469.3	249.0	56.2	6251.6
	Max.	369.6	604.0	805.0	944.0	1014.0	1012.0	931.0	777.0	574.0	330.0	95.0	
	Min.	145.6	258.0	461.0	403.0	494.0	554.0	558.0	284.0	155.0	58.0	16.0	
	S.D.	50.9	71.0	68.7	110.5	104.7	97.8	77.3	85.7	79.0	48.0	16.0	
Diffuse	Mean	120.9	172.9	213.3	238.4	249.0	259.6	240.6	207.9	174.2	116.6	37.3	2030.6
	Max.	183.9	270.0	354.0	432.0	430.0	437.0	403.0	326.0	247.0	158.0	54.0	
	Min.	86.0	117.0	140.0	127.0	124.0	121.0	117.0	111.0	99.0	52.0	14.0	
	S.D.	27.1	40.0	16.0	78.2	80.8	92.2	72.8	53.1	40.0	24.8	8.8	
Direct	Mean	541.7	669.9	740.5	746.0	746.4	725.7	707.1	650.6	509.3	340.8	110.9	6488.9
	Max.	916	954	974	985	987	973	932	864	769	593	283	
	Min.	80	141	220	64	120	159	189	45	35	16	13	
	S.D.	205.8	196.6	179.0	218.0	198.5	206.8	165.4	161.9	164.7	129.0	62.0	

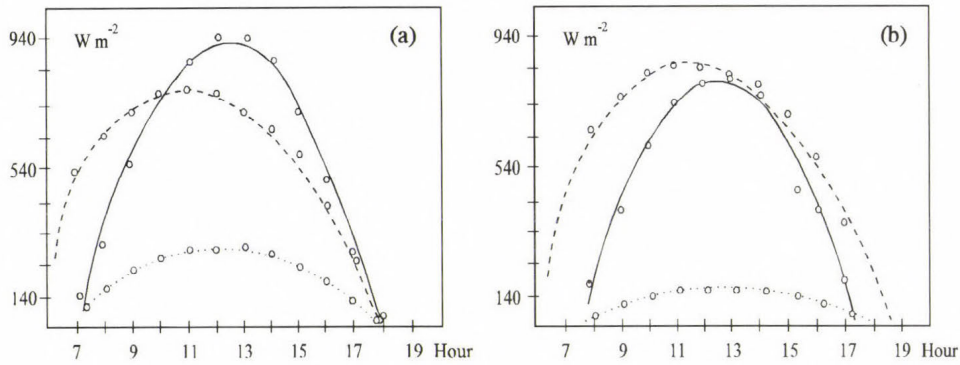

Fig. 1. Mean hourly solar radiation *(a)* for February, *(b)* for March (solid line—global, dotted line—diffuse, dashed line—direct).

$$K = 1.39 - 4.027\,K_T + 5.53\,K_T^2 - 3.108\,K_T^3, \tag{8}$$

where $K=D/G$, $K_T=G/G_0$, G_0 is the daily extraterrestrial, undepleted solar-radiation. The comparison between the values of diffuse ratio K, computed by Eqs. (7) and (8), and the experimental ones has pointed out considerable deviation as displayed in *Fig. 2*. This deviation has been found by other inves-

Table 3. The coefficients a_i, b_i and c_i in Eqs. (4)–(6)

Month	Constant								
	a_1	a_2	a_3	b_1	b_2	b_3	c_1	c_2	c_3
February	-520	-238	346	5660	835	2620	-6000	-886	-3220
March	-334	-393	379	5155	1280	2207	-5548	-1383	-3008

tigators (*Barbaro et al.*, 1981; *Katsoulis* and *Papachristopoulos*, 1978), indicating the important role played by the local influences in the correlation of diffuse radiation with the cloudiness index as has been shown by *LeBaron* and *Dirmhirn* (1983) and *Neuwirth* (1980). In this paper we tried to generate an experimentally derived relationship for Qena, using linear, quadratic and cubic approximations. The best relation was given by the following linear equation

$$K = 1.324 - 1.448\,K_T. \tag{9}$$

The correlation coefficient is 0.98.

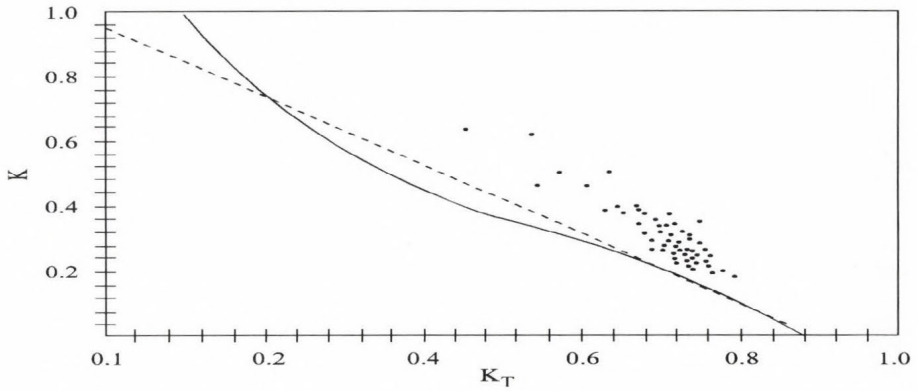

Fig. 2. Relation between daily diffuse ratio K and clearness index K_T.

4. Conclusions

As a first step solar radiation station was established in Qena Upper Egypt, (ideal climate for solar energy projects) to provide information about the available energy in a systematic fashion and with assurances of accuracy. The exposure and installation of the measuring instruments were selected according to the rules given by the World Meteorological Organization.

The analysis of the measurements leads to an empirical model to estimate the global solar radiation with its diffuse and direct components. Correlation between the daily global and diffuse radiation has been studied. The results obtained indicate the effect of locality on the regression formulas. An empirical linear relation was found convenient to fit the measured data in Qena.

The established station will provide intermittently measurements of global and diffuse radiation along with standard meteorological parameters for the future investigations. The data may also serve as a useful reference for system designers and users in other subtropical region of similar climatic conditions.

References

Barbaro, S., Cannata, G., Coppolino, S., Leone, C. and *Sinagra, E.*, 1981: Diffuse solar radiation statistics for Italy. *Solar Energy 26*, 429-435.

WMO, 1983: *Guide to Meteorological Instruments and Method of Observation.* Geneva, Switzerland.

Katsoulis, V.D. and *Papachristopoulos, L.E.*, 1978: Analysis of solar radiation measurements at Athen's observatory and estimates of solar radiation in Greece. *Solar Energy 21*, 217-226.

Klein, S.A., 1977: Calculation of monthly average insolation on tilted surface. *Solar Energy 19*, 325-329.

Latimer, J.R. and *Mac Dowall, J.*, 1971: Radiation measurement, international field year for the Great Lakes. *Technical Manual Series*, No. 2.

LeBaron, B. and *Dirmhirn, I.*, 1983: Strengths

and limitations of the Liu and Jordan model to determine diffuse from global irradiance. *Solar Energy 34*, 167-172.

Lenung, C.T., 1980: The fluctuation of solar irradiance in Hong Kong. *Solar Energy 25*, 485-494.

Liu, Y.H. and *Jordan, R.C.*, 1960: The interrelationship and characteristic distribution of direct, diffuse and total radiation. *Solar Energy 4*, No. 3, 1-19.

Neuwirth, F., 1980: The estimation of global and sky radiation in Austria. *Solar Energy 24*, 421-426.

Page, J.K., 1964: The total estimation of monthly mean values of daily total shortwave radiation on vertical and inclined surfaces from sunshine records for latitude 40°N–40°S. *Proc. UN Conf. New Sources of Energy*, 378-387.

BOOK REVIEW

Wayne, R. P.: **Chemistry of Atmospheres.** Clarendon Press, Oxford. Second edition 1991, reprinted 1992, 1993. pp. 447, 9 chapters.

Since the publication of *Junge*'s classical book on air chemistry in 1963 (Academic Press, New York and London) several volumes have been published on the subject. These volumes differ at least because of two reasons. First, books are different concerning the depth of the discussion of smaller scale air pollution problems. Secondly, some of the books include chapter(s) on ion chemistry in the middle and upper atmosphere, not discussed by *Junge*. Concerning its content and structure the present volume is unique. *Wayne* discusses not only ion chemistry (Chapter 6: *Ions in the atmosphere*) and the chemistry of the airglow (Chapter 7: *The airglow*), but also the properties of *Extraterrestrial atmospheres* (Chapter 8). In addition to this, in Chapter 5 on *The Earth's troposphere* a subsection is devoted to air pollution, while in Chapter 2 (*Atmospheric behaviour as interpreted by physics*) physical and dynamical properties of the Earth's atmosphere are summarized. Consequently, *Wayne*'s publication is the most general textbook of the chemistry of atmospheres (in plural!).

However, the completeness is not the only merit of the author. The text is also clear, relatively short and well-written. This makes the book very useful in teaching the subject at universities according to the author's intentions. The use of the volume by students is facilitated by Chapter 3 which contains the bases of *Photochemistry and kinetics applied to atmospheres.* Further, except figures and tables, literature citations are generally not given in the text. However, very good reference lists follow each chapter, grouped didactically according to subject areas. An other interesting feature of the work reviewed is that the first chapter (*Chemical composition: a preliminary survey*) gives a general survey of the remaining parts of the book. It should be noted that the composition of the Earth's atmosphere is presented in comparison with the gaseous covers of the solar system bodies and the importance of the linkage between the biosphere and the atmosphere on our planet is emphasized. Since the aim of the author is also to present man-made effects on our atmosphere, Chapter 4 entitled *Ozone in Earth's stratosphere* discusses—among other things—ozone trends and the ozone hole problem. In accordance with this aim the last chapter *Evolution and change in atmospheres and climates* contains subsections on the past and future of our atmosphere including possible anthropogenic modifications. In this respect *Wayne* argues that some prospect is the controlled nuclear fusion and he concludes that global warming should

be mitigated by "...harnessing, as a source of energy, the process out of which the Sun, planets and atmospheres were born".

The reviewer believes that even this short discussion is sufficient to demonstrate that the present book is excellent. After reviewing it one can understand why it was published in two editions and the second edition was reprinted two times. Thus, *Wayne's* book is proposed to students, professors and research workers and to everybody who wants to get acquainted easily with the problems of the chemistry of *all* the planets and moons in the Solar System.

E. Mészáros

NEWS

"Science Advice"

Round table discussion in the Club of the Hungarian Academy of Sciences

On 18 January 1994, in the morning, a small round table discussion took place in the Club of the Hungarian Academy of Sciences. The topic was: 'science advice', namely how technical expertise is being provided for decision making in general and in particular in connection with issues such as technological development and environmental change. Participants included the keynote speaker: *Jesse Huntley Ausubel* (Director, Programme for the Human Environment, The Rockefeller University, New York), *Professor Helga Nowotny* (Permanent Fellow, Collegium Budapest), *Professor Ricardo Galli* (Scientific Advisor, Ministry of Universities and Scientific Research, Rome), and a number of Hungarian scientists representing a wide range of disciplines from social to technical sciences, also including meteorology. The round table was chaired by the undersigned.

Jesse Ausubel in his introductory talk provided an outline of the organizational ecology of science advice in America. As he pointed out, one way that the American government has changed in the past 50 years was through the establishment and expansion of organizations providing technical expertise for decision making. He noted that the US government may be these days probably the largest employer of scientists in the world (in 1990 the federal government directly employed 112,000 scientists and 111,000 engineers full-time.)

The vantage point of the keynote speaker from which he overviewed the working of this vast machinery may be considered indeed as quite exceptional. He had been working during the last five years as Director of Studies of the Carnegie Commission on Science, Technology and Government, and this job offered him a particularly deep insight into the whole area. His chosen approach in his keynote lecture was to look at the four essential perspectives identified in the 'cultural theory' of science advice, developed by *Douglas et al.*. Applying this approach he analysed the widely differing views about science advice of the 'elites' (the President and top politicians), the 'bureaucracies', the 'general public', and the 'independent (activist) groups'.

All four perspectives are associated with certain characteristic views on 'science advice' and the corresponding actors (elites, bureaucracies, etc.) all have their own specific views on where the shortcomings of the existing mechanisms for science advice may be. These views are widely divergent and sometimes even conflicting, which may be in itself a very interesting subject for closer analysis.

While we cannot go into the details, it may be interesting to mention here—with special regard to global environmental issues—a strong critical remark about the US research community, which is usually voiced by the so-called 'organized activists'. They say that the research community has become much less independent of the government than it used to be. Hence, they say, there is too much positive feedback at higher levels: the 'Republic of Science' has been corrupted. This opinion encapsulates a polarized conflict of opinion between the 'independents' and the establishment. In activists' views loss of independence means loss of credibility, whereas in the opinion of the elites (and the bureaucracies as well) more independence goes along with less responsibility.

After the keynote lecture the ensuing lively discussion converged on the problems of science advice in Hungary and on comparisons of approaches in America, in Italy and in Hungary. To summarize such debates in a few words is quite impossible. One could only try to highlight some reflections.

The American model of 'science advice' appears to be based on permanent structures and networks, which all continue working and speak up whenever they see a problem, even if unrequested. On the top of this network there are 60 key scientific positions which are strongly rotated among a much larger group of top scientists in reserve.

Opposite to this, in Hungary, science advice is being provided mainly through ad hoc committees which only exist, work and speak if requested, and they only respond to the questions on which they are requested to speak. These ad hoc groups are changing, but the persons involved are often the same. In Italy a revolving door operates between the government, the universities, the research institutes, etc., and thereby provision is made for the necessary rotation. (However, some outstanding personalities tend to be present everywhere and tend to know everything better, which may be a source of difficulties.)

Concerning the Hungarian side, some comments were also made that perhaps the Academy of Sciences could have the potential of providing an independent voice in science advice, thereby to bridge the credibility gap, but it was also noted that currently there may be difficulties in turning this potential into a reality.

Another point made was that—at least in Hungary—proponents of science may be sometime too anxious to combat against everything that is not 'science proper'. In this effort, along with 'bad science', a potential ally, 'proto-science' is often tactlessly also turned away and alienated (a strong enough reason for public anti-science feelings). Perhaps it would be beneficial for the promotion of a truly effective distribution of scientific information and knowledge to embrace more heartily the proto-professional groups (such as teachers of public schools, or science writers and journalists) in some circles of science proper.

In conclusion it may be most fitting to put on record a remark made during the discussion by *Professor Helga Nowotny*: "...internationalization in science tames partisanship". We trust it does, and we confidently hope that the round table discussion summarized above was a step in this direction.

R. Czelnai

ATMOSPHERIC ENVIRONMENT

an international journal

To promote the distribution of Atmospheric Environment *Időjárás* publishes regularly the *contents* of this important journal. For further information the interested reader is asked to contact *Dr. P. Brimblecombe,* School for Environmental Sciences, University of East Anglia, Norwich NR 7TJ, U.K.

Volume 27A Number 17/18 1993

Arctic Air, Snow and Ice Chemistry

Section II: The Arctic Gas and Aerosol Sampling Program (AGASP)

Section III: Arctic snow and ice chemistry

Section IV: Monitoring programs: atmospheric chemistry and meteorology in the Arctic

Volume 28 Number 1 1994

Surface Ozone

A.S. Lefohn: Introduction: The special issue of *Atmospheric Environment* on surface ozone, 1-2.

C. Cartalis and *C. Varotsos*: Surface ozone in Athens, Greece, at the beginning and at the end of twentieth century, 3-8.

S.J. Oltmans and *H. Levy II*: Surface ozone measurements from a global network, 9-24.

Young Sunwoo, G.R. Carmichael and *H. Ueda*: Characteristics of background surface ozone in Japan, 25-37.

J.F. Austin and *R.P. Midgley*: The climatology of the jet stream and stratospheric intrusions of ozone over Japan, 39-52.

T.D. Davies and *E. Schuepbach*: Episodes of high ozone concentrations at the Earth's surface resulting from transport down from the upper troposphere/lower stratosphere: a review and case studies, 53-68.

V.W.J.H. Kirchhoff and *E.V.A. Marinho*: Layer enhancements of tropospheric ozone in regions of biomass burning, 69-74.

J. Staehelin, J. Thundium, R. Buehler, A. Volz-Thomas and *W. Graber*: Trends in surface ozone concentrations at Arosa (Switzerland), 75-87.

U. Pedersen and *A.S. Lefohn*: Characterizing surface ozone concentrations in Norway, 89-101.

T. Laurila and *H. Lättilä*: Surface ozone exposures measured in Finland, 103-114.

J.S. Bower, K.J. Stevenson, G.F.J. Broughton, J.E. Lampert, B.P. Sweeney and *J. Wilken*: Assessing recent surface ozone concentrations in the U.K., 115-128.

J.P. Beck and *P. Greenfelt*: Estimate of ozone production and destruction over northwestern Europe, 129-140.

P.R. Miller, M. de Lourde de Bauer, A.Q. Nolasco and *T.H. Tejeda*: Comparison of ozone exposure characteristics in forested regions near Mexico City and Los Angeles, 141-148.

D. Kley, H. Geiss and *V.A. Mohnen*: Tropospheric ozone at elevated sites and precursor emissions in the United States and Europe, 149-158.

Chung-Ming Liu, Ching-Ya Huang, Shinn-Liang Shieh and *Ching-Chi Wu*: Important meteorological parameters for ozone episodes experienced in the Taipei Basin, 159-173.

Volume 28 Number 2 1994

N.L. Rose and *S. Juggins*: A spatial relationship between carbonaceous particles in lake sediments and sulphur deposition, 177-183.

J.F. Pankov: An absorption model of gas/particle partitioning of organic compounds in the atmosphere, 185-188.

J.F. Pankow: An absorption model of the gas/aerosol partitioning involved in the formation of secondary organic aerosol, 189-193.

J.C. Dechaux, V. Zimmermann and *V. Nollet*: Sensitivity analysis of the requirements of rate coefficients for the operational models of photochemical oxidants formation in the troposphere, 195-211.

H. Akimoto and *H. Narita*: Distribution of SO_2, NO_x and CO_2 emissions from fuel combustion and industrial activities in Asia with $1° \times 1°$ resolution, 213-225.

J.C. Little, A.T. Hodgson and A.J. Gadgil: Modeling emissions of volatile organic compounds from new carpets, 227-234.

Z. Klimont, M. Amann, J. Cofala, F. Gyárfáš, G. Klaassen and *W. Schöpp*: An emission inventory for the Central European Initiative 1988, 235-246.

R.M. Harrision and *I.M. Msibi*: Validation of techniques for fast response measurement of HNO_3 and NH_3 and determination of the $[NH_3]$ $[HNO_3]$ concentration product, 247-255.

Technical Notes

Short Communications

NOTES TO CONTRIBUTORS

The purpose of *Időjárás* is to publish papers in the field of theoretical and applied meteorology. These may be reports on new results of scientific investigations, critical review articles summarizing current problems in certain subject, or shorter contributions dealing with a specific question. Authors may be of any nationality but papers are published only in English.

Papers will be subjected to constructive criticism by unidentified referees.

* * *

The manuscript should meet the following formal requirements:

Title should contain the title of the paper, the names(s) of the author(s) with indication of the name and address of employment.

The title should be followed by an *abstract* containing the aim, method and conclusions of the scientific investigation. After the abstract, the *key-words* of the content of the paper must be given.

Three copies of the manuscript, typed with double space, should be sent to the Editor-in-Chief: *P.O. Box 39, H-1675 Budapest,* Hungary.

References: The text citation should contain the name(s) of the author(s) in Italic letter or underlined and the year of publication. In case of one author: *Miller* (1989), or if the name of the author cannot be fitted into the text: *(Miller,* 1989); in the case of two authors: *Gamov* and *Cleveland* (1973); if there are more than two authors: *Smith et al.* (1990). When referring to several papers published in the same year by the same author, the year of publication should be followed by letters a,b etc. At the end of the paper the list of references should be arranged alphabetically. For an article: the name(s) of author(s) in Italics or underlined, year, title of article, name of journal, volume number (the latter two in Italics or underlined) and pages. E.g. *Nathan, K. K.,* 1986: A note on the relationship between photosynthetically active radiation and cloud amount. *Időjárás 90,* 10-13. For a book: the name(s) of author(s), year, title of the book (all in Italics or underlined with except of the year), publisher and place of publication. E.g. *Junge, C. E.,* 1963: *Air Chemistry and Radioactivity.* Academic Press, New York and London.

Figures should be prepared entirely in black India ink upon transparent paper or copied by a good quality copier. A series of figures should be attached to each copy of the manuscript. The legends of figures should be given on a separate sheet. Photographs of good quality may be provided in black and white.

Tables should be marked by Arabic numbers and provided on separate sheets together with relevant captions. In one table the column number is maximum 13 if possible. One column should not contain more than five characters.

Mathematical formulas and *symbols:* non-Latin letters and hand-written marks should be explained by making marginal notes in pencil.

The final text should be submitted both in manuscript form and on *diskette.* Use standard 3.5" or 5.25" DOS formatted diskettes for this purpose. The following word processors are supported: WordPerfect 5.1, WordPerfect for Windows 5.1, Microsoft Word 5.5, Microsoft Word for Windows 2.0. In all other cases the preferred text format is ASCII.

* * *

Authors receive 30 *reprints* free of charge. Additional reprints may be ordered at the authors' expense when sending back the proofs to the Editorial Office.

Published by the Hungarian Meteorological Service

Budapest, Hungary

INDEX: 26 361

HU ISSN 0324-6329